CHEMISTRY OF MATERIALS

pubs.acs.org/cm

Article

Unleashing the Potential of Fast Charging Batteries: Leveraging Anion Redox Chemistry in Ni- and Co-Free Cathodes

Sudhan Nagarajan, Subhayan Roychoudhury, Conan Weiland, Debora Motta Meira, Mahalingam Balasubramanian, David Prendergast, Sooyeon Hwang, and Leela Mohana Reddy Arava*

Cite This: *Chem. Mater.* 2024, 36, 8623−8638

Read Online

ACCESS | Metrics & More | Article Recommendations | Supporting Information

ABSTRACT: Designing Li-ion battery cathodes free of critical raw materials such as Co and Ni has a huge technological and societal impact. Although anion redox-based Li-rich oxide cathodes allow for designing Co- and Ni-free cathode compositions, the Li-rich oxides demonstrated voltage fade, voltage hysteresis, and irreversible oxygen release despite their high capacity. Conversely, anion redox through highly covalent chalcogenides (S/Se) is emerging due to the improved covalency between metal *d* and ligand *p* bands. Here, we investigate the tuning of multichalcogen (S/Se) *p* band and redox-active metal *d* band in a model Li-rich chalcogen composition, $Li_{1.13}Ti_{0.57}Fe_{0.3}S_{2-y}Se_y$ (y = 0−1), through in-depth electrochemical, X-ray spectroscopy, and DFT-based electronic structure investigations. Introducing the appropriate amount of Se *p* band character in anion redox sulfides increases the interlayer distance and metal−ligand covalency without modifying the original crystal structure, promoting significant electrochemical reversibility through mixed anionic (Se^{2-}/Se^{n-}, S^{2-}/S^{n-}, wherein n < 2) and cationic (Fe^{2+}/Fe^{3+}) redox reactions. We show the detailed Fe, S, and Se redox contributions during Li insertion−extraction through X-ray absorption (XAS) and hard X-ray photoemission spectroscopy (HAXPES) measurements. The orbital tuning approach improves the rate capability for more than 10C charge−discharge rate, exhibiting more than 50% of its original capacity obtained at the C/20 rate. The buffer cation in the lattice (Ti^{4+}) remains electrochemically inactive even after significant Se *p* band introduction in the sulfide framework. Overall, this work takes advantage of multianion redox chemistry to uncover practically demanding fast charging−discharging characteristics in intercalation cathodes. The obtained knowledge of this design can be extended to other oxide and chalcogen cathodes for high-performance Li-ion batteries.

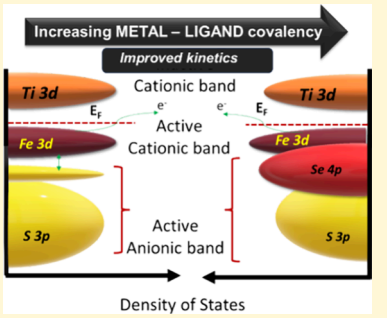

INTRODUCTION

The environmental and ethical issues from both Ni and Co mining present a formidable technological challenge, that is, to develop technologies with limited reliance on Ni and Co Li-ion cathodes while maintaining high performance and supply chain stability[1,2] However, the state-of-the-art cathode materials (Ni- and Co-based oxides) are already approaching their theoretical limits, especially because most of the current cathode materials' specific capacity is limited to 180−200 mAh/g.[3−6] The inherent challenge of the Li-ion batteries attracted the battery community to develop high Ni and low/zero Co cathodes for high capacity and derisking the Co supply chain issues. Compared to Co, battery-grade Ni production also faces environmental, societal, and supply chain risks despite possessing a larger distribution of Ni than that of Co.[7] To solve this cobalt-led conundrum, a fundamental solution is to develop high-performance battery chemistry that is free from critical raw materials such as Ni and Co but without compromising significant performance metrics. However, complete elimination of these elements in cathode materials has trade-offs in terms of performance and stability, but a few other alternative redox chemistry cathodes with limited critical elements are emerging.[8−10]

With this motivation, a multielectron Li-rich cathode chemistry was introduced to the battery community, which leverages both cationic and anionic redox during Li extraction and offers significant advantages in enhancing specific capacity and energy density of the current cathode materials.[6,11,12] However, anion redox cathode chemistry is not straightforward as it goes through a complex redox reaction pathway and is limited by sluggish kinetics, leading to fundamental issues such as voltage fade, voltage hysteresis, and irreversible oxygen release.[13−16] Understanding these issues took more than a decade of research,[17−22] and the fundamental driving force for achieving anionic redox is the tuning of covalency between the metal and ligand present in the cathode structural framework. During anionic redox participation, the hole stabilization on the anions will also impact the reversible anionic redox reaction; otherwise, the anions such as O^{2-} will be released as

Received: March 22, 2024
Revised: July 17, 2024
Accepted: July 18, 2024
Published: September 3, 2024

molecular oxygen (O_2) from the crystal lattice.[23] This is the reason why the complex O^{2-} anion redox stabilization demonstrated better efficiency in the covalent (orbital tightness between metal and oxygen) Ru−O and Ir−O metal−ligand environment compared to the Mn−O environment.[24−27] The investigations of model compounds significantly improved our understanding of anion redox chemistry, but the Ru- and Ir-based compositions are impractical because of their cost.

Hence, an alternative approach of replacing oxygen ligands with sulfide ligands in cathode materials has gained attention due to the availability of a wide range of metal and chalcogen ligand environments for efficient anionic redox stabilization. In early works, Rouxel investigated anion−cation redox competition in various metal−ligand environments, laying a strong foundation for exploring recent chalcogen anion redox cathode chemistry.[28,29] With this background, chalcogen anion redox cathode chemistry was demonstrated recently in various structural frameworks, especially the seminal works of antiperovskite, Li_2TiS_3-based layered Li-rich cathode materials.[30−32] The establishment of improved metal−ligand covalency is the key to achieve reversible sulfide anionic redox reactions in various chalcogen structural frameworks.[33,34]

In anion redox cathodes, one of the major concerns is their sluggish kinetics and slow rate capability, related to bottlenecks for transport of Li ions in the lattice. In addition to limited material availability, fast charging is not common in materials, especially cathode materials, mainly due to the lack of material understanding and solution to the origin of fast charging. With this motivation, addressing sluggish anion redox kinetics by increasing the electronic interaction between chalcogen ligands (O, S, Se, and Te) and metals (d and p orbital metals) through exploiting metal−ligand covalency properties is a promising avenue to develop highly reversible anion redox cathodes.

Despite the previous approaches of tuning metal−ligand covalency, (e.g., Se mixing in the sulfide framework), the introduction of highly covalent metal−ligand states (Se 4p states into a sulfide framework) in the presence of both buffer cations (d^0: empty d states) and redox-active (d^n: partially filled d states) cations has not yet been evaluated with the goal of unlocking high rate electrochemical reversibility. For example, substitution of Se^{2-} in the sulfide framework detrimentally affected the layered structure, leading to poor electrochemical reversibility.[34] In another case, redox couple evolution was witnessed during electrochemical reactions, leading to triggering anion redox in Li_2TiS_3.[35] Considering this research direction, the tuning of metal−ligand covalency using Se 4p introduction near S 3p states on the chalcogen structure needs to be deeply investigated to explore their electrochemical interaction toward achieving improved anion redox reversibility.

Therefore, in this proof-of-concept work, we provide a systematic investigation to take advantage of the emerging chalcogen anion redox chemistry in uncovering the potential benefits of high-rate electrochemistry features in intercalation-based cathodes for Li-ion batteries. We demonstrate this idea in a model chalcogen composition [$Li_{1.13}Ti_{0.57}Fe_{0.3}S_{2-y}Se_y$ (y = 0−1)] using Se 4p incorporation in the sulfide lattice to explore its effect on high-rate reversibility, lithiation/delithiation kinetics, and charge compensation mechanisms through fundamental electrochemistry, synchrotron spectroscopy, and electronic structure calculations. Understanding the origin of improved reversibility and the appropriate charge compensating mechanisms will lead to developing alternative and fast rate capable cathode chemistries with less reliance on critical battery materials such as Ni and Co.

EXPERIMENTAL SECTION

Material Synthesis. The following chemicals were used as received for the synthesis: Li_2S (Sigma-Aldrich, 99.9%), Ti (Alfa Aesar, 99%), Se (Alfa Aesar, 99.999%), S (Alfa Aesar 99.5%), and FeS (Alfa Aesar, 99%). Li_2S, FeS, Ti, S, and Se precursors were stoichiometrically taken to achieve this $Li_{1.13}Ti_{0.57}Fe_{0.3}S_{2-y}Se_y$ formula ($0 \leq y \leq 1$). Further, the mixture was ground well using an agate mortar and pestle for 30 min inside an Ar-filled glovebox (O_2 < 1 ppm, H_2O < 0.1 ppm). The precursors were loaded into a carbon-coated quartz tube and heat sealed under a vacuum condition (~10^{-3} mbar). The ampule was heated to 750 °C at a heating rate of 40 °C/h followed by dwelling for 36 h and cooled to room temperature at 40 °C/h. Black-colored crystals for the pristine and Se-doped samples were obtained and stored inside a glovebox for further characterization. Here, we attempted to systematically dope Se^{2-} in S^{2-} sites to activate mixed cationic ($Fe^{2+/3+}$) and anionic (S/Se) redox reactions.

X-ray powder Diffraction. X-ray powder diffraction (XRD) was conducted using a Bruker D8 ADVANCE diffractometer using Cu Kα radiation (λ = 1.54 Å) in the 2θ range from 10 to 80°. To avoid air exposure to the samples, the measurement was carried out using a sealed Kapton capillary (Cole Parmer/1 mm capillary) filled with active materials.

Electrochemical Characterization. All of the electrode preparation was performed in an argon-filled glovebox. All of the electrodes were prepared by a slurry coating method. The electrode slurry was prepared by mixing active material, conductive carbon (C65, MTI), and poly(vinylidene fluoride) (PVDF) binder (Sigma-Aldrich) in a ratio of 80:15:05 using N-methyl-2-pyrrlidinone (NMP, 99.5%; Sigma-Aldrich) as solvent. The homogeneous mixture was cast on a conductive carbon-coated aluminum current collector (MTI). The coated electrodes were dried at 80 °C in a vacuum heating chamber inside the glovebox for at least 12 h. Finally, the electrodes were cut into circles and yielded a loading of ~3 mg on each electrode. All electrochemical analyses were performed in conventional coin cells (CR2032, SS316, MTI) and the cells were prepared in an Ar-filled glovebox (O_2 < 1 ppm, H_2O < 0.1 ppm). Li foil (750 μm, Alfa Aesar) was used as anode, and its surface was cleaned using razor blades; a trilayer Celgard membrane was used as separator. A commercial 1 M lithium hexafluorophosphate ($LiPF_6$) in an ethylene carbonate (EC)/dimethyl carbonate (DMC) mixture (50/50 ratio by volume) was used as the electrolyte (Sigma-Aldrich). All the galvanostatic tests were performed either on an Arbin battery cycler (BT-2043) or a Landt instrument at appropriate current density values. The specific capacity was calculated for all electrodes based on the active material loading in the cathode. All cyclic voltametric and galvanostatic intermittent titration technique (GITT) studies were carried out using a Biologic SP-300 potentiostat.

Microscopy Investigation. The high-resolution transmission electron microscope (HR-TEM), and high angle annular dark field-scanning transmission electron microscope (HAADF-STEM) were used at the Center for Functional Nanomaterials, Brookhaven National Laboratory. For all of the microscopy experiments, once the targeted electrodes attained the desired state of charge, the electrode materials were collected from the Al current collector. The collected particles were sonicated in a vial with anhydrous DMC to ensure uniform dispersion prior to drop casting on a lacey carbon-coated TEM grid. Extreme care was taken to avoid air exposure of the samples, and the sample preparation was carried out in an Ar-filled glovebox. The bright-field HR-TEM was obtained with a JEOL JEM-2100F TEM instrument at an accelerating voltage of 200 kV. The HAADF-STEM and STEM-EDX elemental maps were acquired by using a Thermo Fisher Scientific Talos F200X with a super-X EDS detection system at an accelerating voltage of 200 kV.

Ex Situ X-ray Absorption Spectroscopy. Ex situ X-ray absorption spectroscopy measurements were performed at the

https://doi.org/10.1021/acs.chemmater.4c00854
Chem. Mater. 2024, 36, 8623−8638

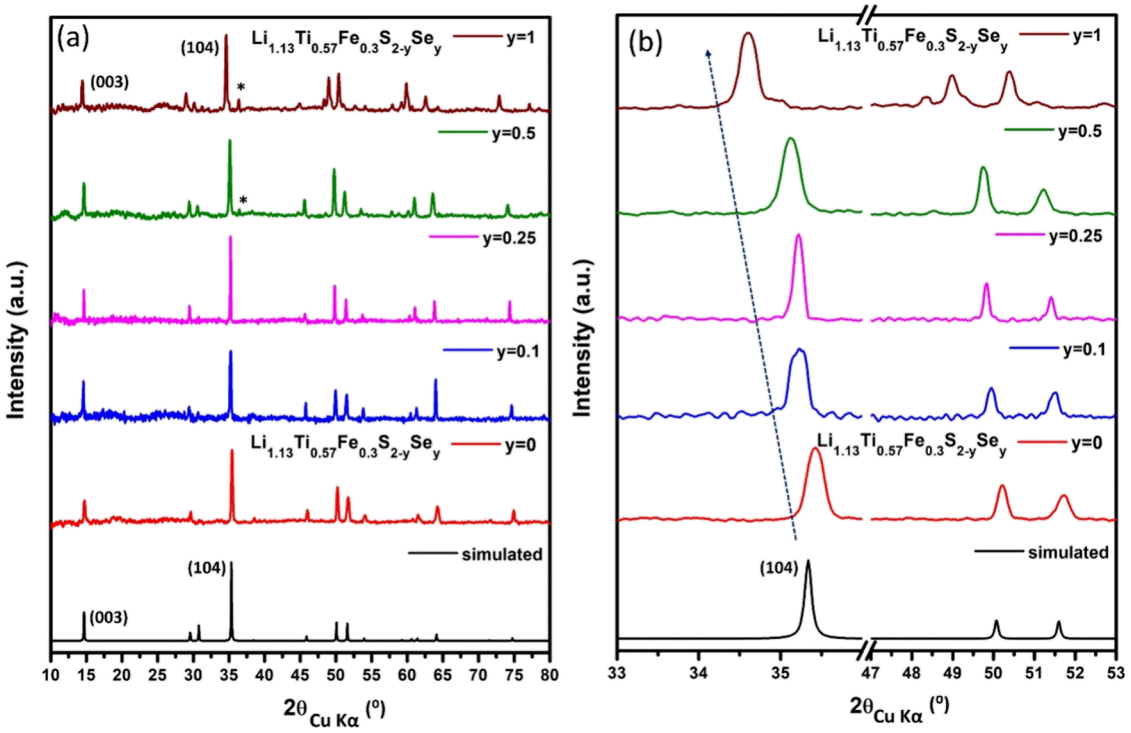

Figure 1. X-ray diffraction patterns of different compositions. (a) XRD profiles of $Li_{1.13}Ti_{0.57}Fe_{0.3}S_{2-y}Se_y$, wherein y = 0.1, 0.25, 0.5, and 1, and the simulated XRD pattern of $Li_{1.13}Ti_{0.57}Fe_{0.3}S_2$. (b) Zoom-in version of the XRD patterns. Arrow denotes the systematic shift of the pattens to the left due to lattice expansion (*possibly metal selenide impurity).

Advanced Photon Source beamline 20-BM-B at the Argonne National Laboratory. The incident beam energy was monochromatized by a Si (111) crystal monochromator. The energy calibration was performed by simultaneously measuring the Se and Fe metal foils. The spectra were acquired in transmission mode using a gas ionization chamber as detector. Once the coin cells attained their desired state of charge, they were collected from the coin cells and washed with DMC three times inside a glovebox. After complete drying, the collected electrodes were sandwiched between Kapton films and pasted onto an appropriate beamline sample plate. The sealed samples were sent to the beamline end station while completely avoiding air exposure. The Se and Fe K-edge data were processed (normalization, calibration, and energy alignment) with the ATHENA software package.[36] All Fe K-edge spectra were energy aligned with respect to the first derivative peak of the Fe reference foil at 7110.75 eV as described in Kraft et al.[37]

HAXPES and NEXAFS Investigation. The HAXPES measurements were performed at the National Institute of Standard and Technology beamline 7-ID-2 (SST-2) of the National Synchrotron Light source II at Brookhaven National Laboratory. A 400 mm diameter concentric hemispherical analyzer, oriented parallel to the photon polarization axis and perpendicular to the photon propagation axis, was used. The HAXPES experiments were carried out using a 3100 eV photon energy. The 3100 eV photon energy selection was achieved using a double Si (111) crystal monochromator, and the measurement was carried out with a pass energy of 100 eV. Samples were mounted at a 10° incident angle for an 80° takeoff angle. S and Ti K-edge measurements were collected at the same end station using the sample drain current normalized to the beam intensity collected from a 1 μm-thick Al foil just upstream of the end station. For both HAXPES and NEXAFS measurements, an unfocused X-ray beam was used and slit down to a size of approximately 0.5 × 0.5 mm. For NEXAFS, samples were mounted for normal incidence.

DFT Calculation. The spin-polarized DFT calculations were carried out based on the projected augmented wave (PAW) method using the Vienna Ab initio Simulation Package (VASP) program. The Perdew−Burke−Ernzerhof (PBE) generalized-gradient approximation (GGA) was used for exchange and correlation. Unit cell volume, shape, and ionic positions of all atoms in the 3 × 3 × 2 super cell ($Li_{60}Ti_{30}Fe_{18}S_{108}$, nothing but $Li_{1.11}Ti_{0.55}Fe_{0.33}S_2$) were allowed to relax until the total energy and forces on the atoms were less than 10^{-5} eV and 0.02 eV/Å, respectively. The constructed model is in close approximation with the experimental composition $Li_{1.13}Ti_{0.57}Fe_{0.3}S_2$. Further, the constructed model was substituted with an appropriate amount of Se atoms to achieve the composition of $Li_{1.11}Ti_{0.55}Fe_{0.33}S_{2-y}Se_y$ (y = 0, 0.22, 0.55, and 1). The plane wave cutoff energy of 520 eV was used in this study. Based on the spin-polarized calculations, the antiferromagnetic ordering exhibited a lower energy than the ferromagnetic ordering. For the antiferromagnetic (AFM) ordering, nine Fe atoms in the structure were initialized with a magnetic moment of ±4 for spin-polarized calculations. On the other hand, all 18 Fe atoms in the structure were initialized with a magnetic moment of 4 for ferromagnetic (FM) spin-polarized calculations. A Hubbard U value of 1.9 eV for Fe atoms was used in this study, as previously used for similar chalcogenide systems.[31] Further, the AFM structure model with Se atoms according to the required stoichiometry was relaxed using the above parameters. After the required threshold was achieved, a single point self-consistent calculation (SCF) was performed. The total energy values of the Se-substituted structures were compared to those of the parent structure. The projected density of states plots for the different structures were obtained using the VASPKIT package. Bader atomic charges were calculated based on the code developed by the Henkelman group.[38]

Simulation Method for Se K-Edge. Simulations of the representative Se K-edge peaks, as shown in Figure 8, are performed within the full core-hole (FCH) approximation,[39] whereby the Kohn−Sham (KS) single-particle energies and orbitals for the core-excited state are obtained from an FCH calculation that simulates the self-consistent field of a positively charged core-ionized state with the help of an appropriately modified pseudopotential. More specifically, the absorption amplitude for exciting an electron from the core orbital $|\phi_0\rangle$ of the ground state to the conduction orbital $|\phi_f\rangle$ of the core-excited state is calculated as $\langle\phi_0|\hat{o}|\phi_f\rangle$, with the corresponding energy being $E^{\mathrm{Tot}}{}_{\mathrm{FCH}} + \epsilon_f - E^{\mathrm{Tot}}{}_{\mathrm{GS}}$, where $\hat{o}$ denotes the dipole transition

https://doi.org/10.1021/acs.chemmater.4c00854
Chem. Mater. 2024, 36, 8623−8638

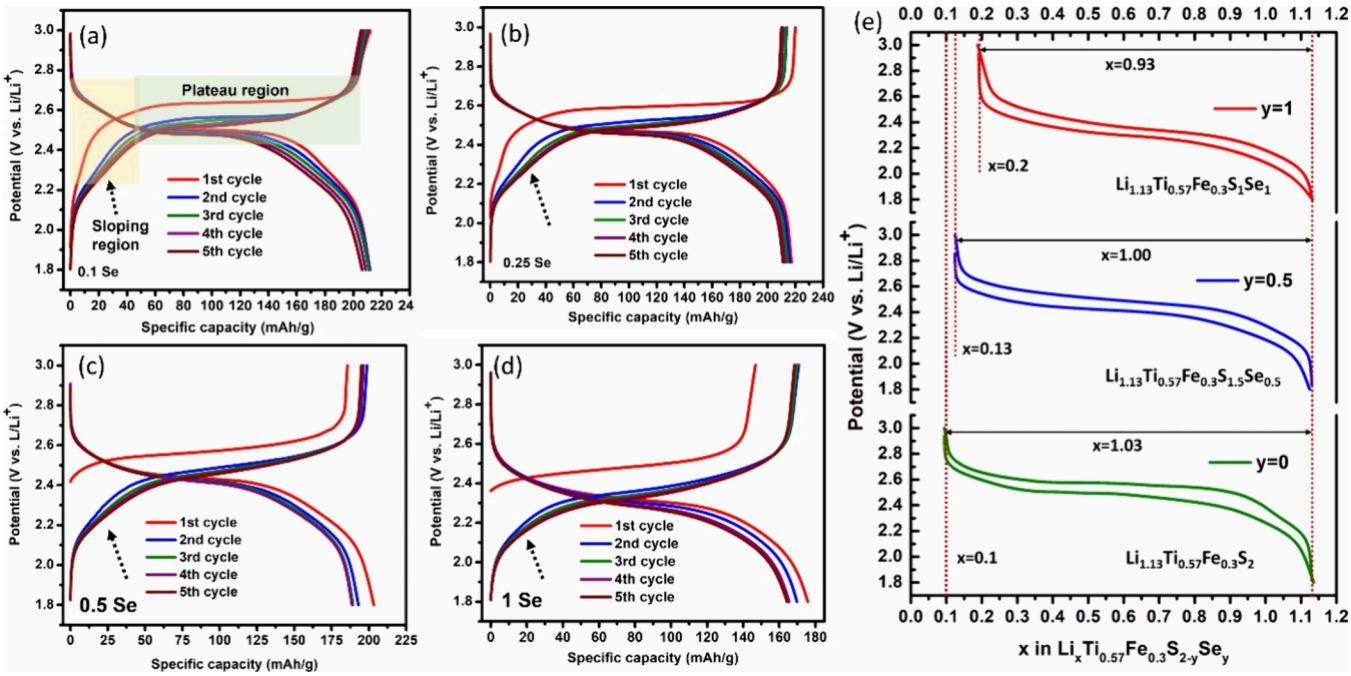

Figure 2. Electrochemical performance of $Li_{1.13}Ti_{0.57}Fe_{0.3}S_{2-y}Se_y$ (y = 0.1, 0.25, 0.5, and 1) cathode materials tested against Li metal reference electrode at 10 mA/g current density. Galvanostatic charge−discharge profiles of (a) y = 0.1 Se, (b) y = 0.25 Se, (c) y = 0.5 Se, and (d) y = 1 Se at 10 mA/g current density. (e) Voltage hysteresis profiles of y = 0, 0.5, and 1 compositions. The voltage hysteresis was plotted using the third cycle of galvanostatic charge−discharge profiles. All electrochemical tests were conducted using 1 M $LiPF_6$ in EC/DMC (50/50, v/v) at room temperature.

operator, ϵ_f is the KS energy of $|\phi_f\rangle$, and E^{Tot}_{GS} and E^{Tot}_{FCH} denote the total energy of the ground and the FCH state, respectively. Because the use of pseudopotential renders the ground and FCH-state energies incomparable, a rigid energy shift, which is unchanged between the lithiated and delithiated systems, is applied to the simulated spectra. For the Se K-edge simulations, the DFT calculations were performed using the Quantum ESPRESSO package.[40] The MBXAS software[41] was used to calculate the spectra.

RESULTS AND DISCUSSION

Structural Investigation. Initially, Li-rich transition metal sulfides and Se-substituted compositions were synthesized by a conventional high-temperature solid-state synthesis using Li_2S, Ti, FeS, S, and Se as precursors (details in the methods). The synthesis was carried out in a carbon-coated quartz tube sealed under a vacuum. Carbon coating in the quartz ampules is used to prevent alkali metal reactions with the quartz ampules at high temperatures. The sealed ampule with cathode precursors is shown in Figure S1a. Originally, the X-ray diffraction (XRD) pattern of the parent compound (Fe substituted Li_2TiS_3) was simulated using the crystallographic information provided by Saha et al.[31] The composition was crystallized into an R-3m space group, and the structure is a derivative structure of Li_2TiS_3, which is a Li-rich layered structural framework with a $C2/m$ space group. In this structure, a lithium layer is sandwiched between two transition metal layers. Ti and Li ions are octahedrally coordinated, and excess Li ions partially occupy Ti positions in the transition metal layer. Lithium ions residing in the lithium layer are extracted when delithiation occurs during charging. Using this parent structure, Se-substituted compositions ($Li_{1.13}Ti_{0.57}Fe_{0.3}S_{2-y}Se_y$, wherein y = 0.1, 0.25, 0.5, and 1) were stoichiometrically prepared to understand electrochemical and electronic structural properties originated from mixed anionic and cationic redox reactions. The XRD patterns of the as-synthesized parent composition along with its simulated powder pattern and Se-substituted compositions are shown in Figure 1a. X-ray powder diffraction was carried out using a capillary tube (1 mm inner diameter) to avoid air exposure during data collection. After the controlled Se substitution, the XRD patterns of the Se added compositions showed negligible changes in the diffraction patterns. However, the Bragg peaks progressively shifted to lower angles (e.g., (104) reflection: 35.42 to 34.60°) as Se content increases (Figure 1b), indicating that the Se addition is not changing the crystal structure and symmetry but leading to lattice expansion, as expected from the increase in atomic radius of Se compared to S. Unlike lower Se compositions, a few additional peaks emerged in the XRD pattern of the high Se content composition (y = 0.5 and 1) that may be due to impurity phases. Furthermore, a homogeneous distribution of Ti, Fe, S, and Se in the different compositions was qualitatively confirmed by scanning transmission electron microscopy-energy dispersive X-ray spectroscopy (STEM-EDX) elemental mapping, as shown in Figures S2 and S3. After the structural purity was confirmed, all of the Se compositions were subjected to electrochemical lithiation (discharge) and delithiation (charge) investigations.

Electrochemical Investigation of Mixed Anionic and Cationic Redox. To understand the effect of Se substitution in the sulfide framework, a detailed electrochemical analysis was carried out in different Se-substituted compositions ($Li_{1.13}Ti_{0.57}Fe_{0.3}S_{2-y}Se_y$, wherein y = 0.1, 0.25, 0.5, and 1). Figure 2 shows the galvanostatic charge−discharge profiles of the Se-substituted compositions. The voltage profiles demonstrate reversible lithium storage behavior without any significant irreversibility in the potential region of 1.8 to 3 V vs Li in this study. The observed charge profiles in some of the compositions are lower than the discharge profiles, which can be attributed to the Li deficiency caused by the high-temperature solid-state synthesis. This Li-deficient nature of

https://doi.org/10.1021/acs.chemmater.4c00854
Chem. Mater. 2024, 36, 8623−8638

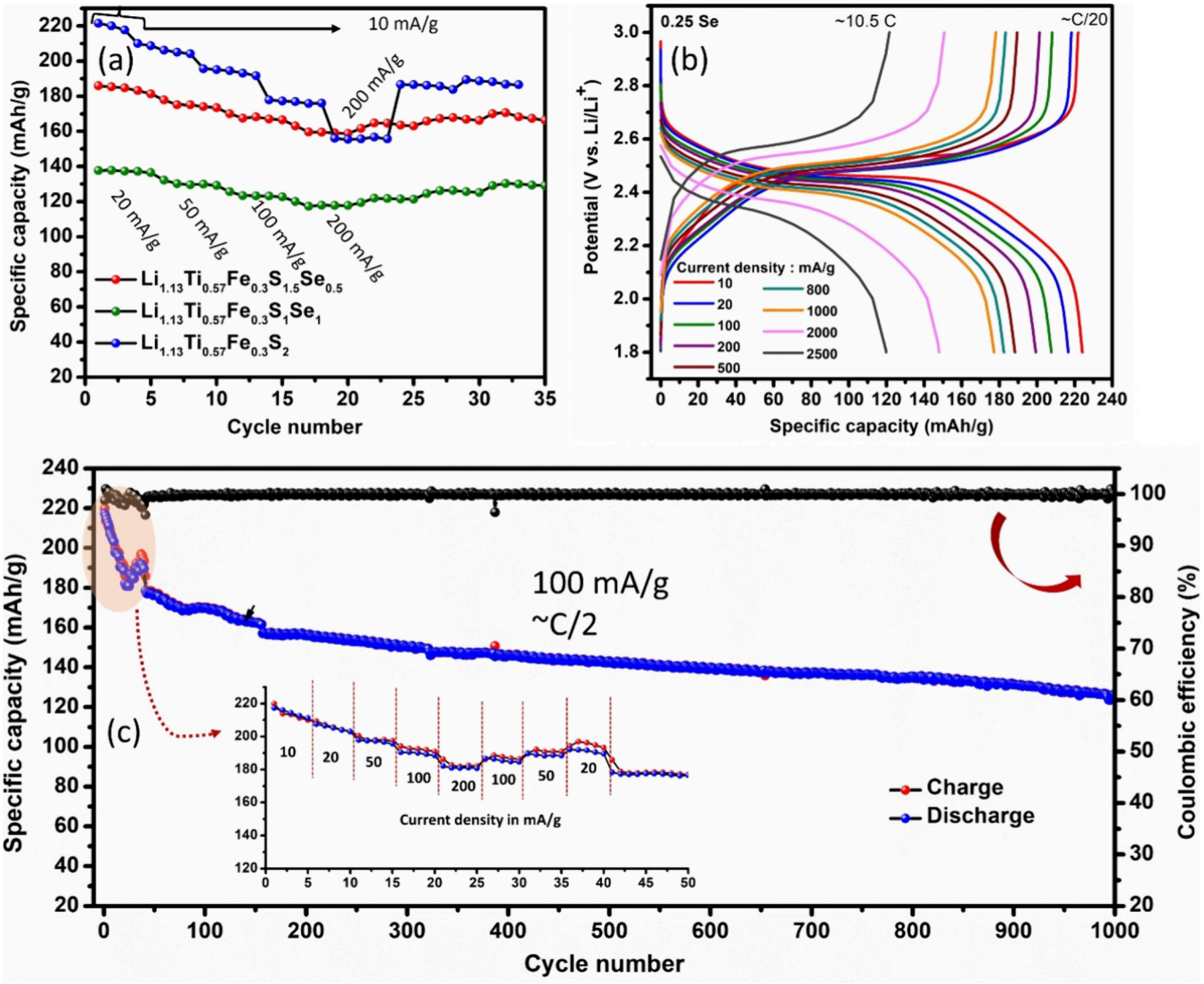

Figure 3. Electrochemical performance of $Li_{1.13}Ti_{0.57}Fe_{0.3}S_{2-y}Se_y$ cathode materials tested against Li metal reference electrode. (a) Rate performance of $Li_{1.13}Ti_{0.57}Fe_{0.3}S_{2-y}Se_y$ composition (y = 0, 0.5, and 1). The lowest current density is 10 mA/g, and the highest current density is 200 mA/g). (b) Galvanostatic charge−discharge profiles of y = 0.25 composition. (c) Cycling stability of y = 0.25 composition at 100 mA/g current density. Inset: first 40 cycles with different current densities.

alkali metal chalcogenides has been discussed by Goodenough and Kim's early research and our recently published work.[33,42] This observation disappears after subsequent cycles, which allows for a sufficient amount of Li ions to be inserted and extracted within the potential range. In addition, the voltage profiles look similar in the Se-substituted compositions, but a slight voltage fade has been noted in the first five continuous charge−discharge cycles at a low current density of 10 mA/g. This phenomenon is due to the mixed anionic and cationic redox chemistry that changes the local environment of the materials during the initial electrochemical reactions, as demonstrated by the difference between the first and second cycles in charge profiles. The Se-substituted compositions exhibited less capacity(for y = 1, ∼ 180 mAh/g) and less redox voltage compared to a similar Li-rich chalcogen composition published by Saha et al.[31] After Se substitution, the local electronic structure of the sulfide framework was modified, and this modulation shifted the redox behavior to a lower potential when increasing the Se content. A similar observation has been witnessed previously by Martinolich et al. in Li_2FeS_2, where the Se substitution approach was used to control the covalency and redox potential behavior, but the strategy detrimentally affected the parent sulfide framework.[34]

By close observation of the charge−discharge profiles, there are two significant regions: a low-voltage sloping region followed by a plateau region (Figure 2a−d). This similar behavior was observed in other mixed cationic and anionic redox chemistry in oxygen anion redox compositions.[20,43] Considering this phenomenon, we assume that a similar behavior is replicated in the Se-substituted compositions, and this understanding is further elucidated with the detailed spectroscopy investigations later in this study. Interestingly, there is a clear trend that the Se addition progressively shifts the observed voltage profiles, but the sloping region is affected significantly by the Se content. The shift in the redox potential was confirmed with the dQ/dV plot in which the dQ/dV curves shifted systematically to low voltage as the Se content increased (Figure S4). Further, the difference in voltage profiles of all Se-substituted compositions (y = 0−1) is shown in Figure S5. A table containing theoretical capacity and

https://doi.org/10.1021/acs.chemmater.4c00854
Chem. Mater. 2024, 36, 8623−8638

experimentally achieved capacity values is shown in Table S1 (Supplementary Note 1). Capacity values of 220 and 180 mAh/g were achieved for low and high Se content compositions, respectively. In Figure 2e, the amount of Li extraction and its associated voltage hysteresis are compared in selected chalcogenide compositions (y = 0, 0.5, and 1). It is evident that the Se substitution reduces the Li extraction gradually, and the voltage hysteresis is not impacted significantly in the potential region used in this study. In these materials, the Li extraction is believed to be compensated by cationic $Fe^{2+/3+}$ redox and chalcogen anionic redox [S^{2-}/S^{n-}, Se^{2-}/Se^{n-}, wherein $n < 2$] reactions. The Ti cation is present in a tetravalent state [Ti^{4+} - $3d^0$ ($t_{2g}{}^0$ $e_g{}^0$)], so it is believed that this cation is not involved in the electrochemical reaction in the potential region used in this study. However, increasing the lower cutoff potential will lead to more Li insertion by compensating electrons from lower Ti^{n+} ($n < 4$) redox couple evolutions. However, this may lead to other complexities such as structural instability and further irreversible electrochemical reactions. To avoid these complexities, the potential region of 1.8−3 V vs Li was used throughout this work even after different Se substitutions, and this in turn may have limited the accessible capacity because the overall potential has dropped with Se substitution. The low specific capacity of the Se-substituted materials is due to the charge population in the S/Se environment in the electronic structure of the materials. When the Se content is increased, the specific capacity is lowered because of the addition of heavier atoms (change in density) without a very large change in unit cell volume (gravimetric capacity).

The rate performance of the cathodes with different Se contents is shown in Figure 3a. Interestingly, the high Se-substituted cathode (y = 1) demonstrates high-rate capability even at a high current density of 200 mA/g (more than 1C for y = 1, ∼185 mA/g is 1C) compared to the zero Se (y = 0) cathode (Figure 3a). It is seen that the high Se-substituted composition possesses less difference between low-rate and high-rate cycling conditions, and the capacity of the cathode after 200 mA/g current density is almost recovered at a low current density of 20 mAh/g (Figure 3a). The rate capability is important for developing fast charging Li storage materials, and this chalcogen family cathodes can be explored for solid-state batteries with high ionic conductive chalcogen solid ionic conductors such as Li_3PS_4 and Li_6PS_5Cl.[44,45] Based on the electrochemical results, adding more Se in the sulfide framework leads to low gravimetric capacity but improves the rate capability. The improvement in the rate performance is not simply because Se possesses higher electronic conductivity than S. The major reason for the improved rate performance is that Se substitution for S improves metal−ligand covalency and expands crystal lattice along the c axis, leading to improved Li-ion transport mechanism.[46] In addition, the improved kinetics can be explained with a possible polaron transport mechanism in ionic crystals. Similar to polaronic conductors, a formation of small polarons can lead to local lattice distortion, and the formation and migration of polarons affect the insertion and diffusion of Li ions as previously proven by several studies for various TM oxide cathodes such as $LiFePO_4$ and Li_2FeSiO_4.[47,48] To efficiently utilize the high rate property of Se-substituted cathodes, we decided to add a minimum Se content to the sulfide framework without compromising the average voltage and specific capacity (Figure S5). Therefore, additional Se added compositions of 0.1 and 0.25 were tested for rate performance followed by cycling stability. Figure 3b shows voltage profiles of the 0.25 Se-substituted cathode at different current densities starting from ∼C/20 (10 mA/g) to more than ∼10 C (2500 mA/g). Interestingly, the kinetic polarization of the observed voltage profiles at different current densities seems to be minimal, indicating that the rate performance is an intrinsic behavior of the material rather than the sole correlation of electronic conductivity (ohmic polarization) of the materials. Even after high-rate testing (inset: first 40 cycles), the 0.25 Se-substituted composition exhibits reasonable reversibility for 1000 continuous charge−discharge cycles with gradual capacity decay (Figure 3c) in Li half-cell configuration. Further, electrochemically important compositions (y = 0.1 and 0.25) were evaluated for rate dependency (up to 10C) with zero Se content followed by cycling stability at 100 mA/g (approximately C/2) (Figure S11a,b). Compared to the 0 Se composition, 0.1 Se and 0.25 Se exhibit moderate stability even after handling an extremely high rate for about more than 10C, confirming that the Se addition can modify the electronic structure of the sulfide framework for achieving a better rate capability and cycling stability. Further, cyclic voltammetry curves of $Li_{1.13}Ti_{0.57}Fe_{0.3}S_{2-y}Se_y$ (y = 0.1, 0.25,0.5, and 1) compositions at different scan rates are shown in Figure S10. It is evident that the cationic redox peak is visible at low Se configurations compared to high Se compositions, agreeing well with the observed galvanostatic voltage profiles (Figure 2a−d). Further, kinetic properties of the different Se-substituted compositions were supported with GITT measurements (Figures S6−S8, Supplementary Note 2). Conventionally, anion redox is highly argued in oxide cathodes where the anion redox stability is highly questionable, and fundamental issues such as voltage fade, voltage hysteresis, and irreversible oxygen release are prevalent during continuous charge−discharge cycling.[13] Conversely, chalcogen anion redox demonstrates superior properties in terms of reduced voltage fade and voltage hysteresis in one of the seminal Li-rich compositions.[31] On the other hand, all other chalcogen compositions even in sulfide frameworks exhibit a moderate cycle life even after nanosizing or surface modification procedures.[32,34,35,49,50] As previously mentioned, Martinolich et al. demonstrated Se addition in Li_2FeS_2 frameworks, but the electrochemical performance and reversibility are subjected to drastic capacity degradation after Se substitution.[34] Originally, this composition was studied for lithiation properties in 1981 by Dugast et al., and a few other groups investigated the same composition for Li storage properties.[51−53] Considering the existing (S) chalcogen anion redox work, the Se-substituted cathode in our work delivers high reversibility and rate performance, suggesting that an appropriate amount of Se incorporation in chalcogen frameworks can be further explored for achieving highly stable cathode materials.

Lattice Stability through Microscopy Investigation. High-resolution transmission electron microscopy (HR-TEM) images were collected to visualize particle morphology and its evolution after the electrochemical reaction. Low-magnification images depict micrometer-sized cathode particles of high Se substitution. The particles before and after electrochemical reactions are illustrated in Figure 4a,b, respectively. Further, high-magnification images confirm the ordered nature of the Se-substituted cathodes, but the corrugated surface region is mainly due to surface contamination. Similarly, the electrochemically discharged cathode particles also exhibit high

https://doi.org/10.1021/acs.chemmater.4c00854
Chem. Mater. 2024, 36, 8623−8638

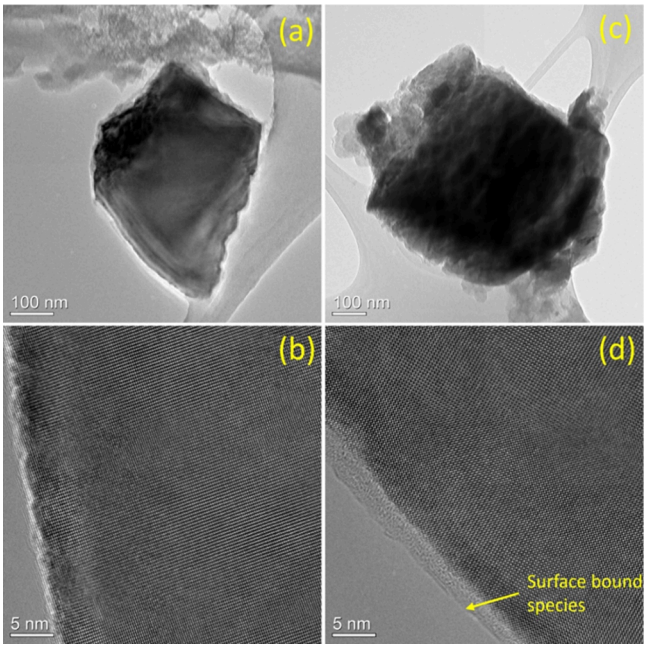

Figure 4. HRTEM images of the $Li_{1.13}Ti_{0.57}Fe_{0.3}S_1Se_1$ cathode material tested against the Li metal reference electrode. (a) Low magnification of the pristine cathode. (b) High magnification of the pristine cathode. (c) Low magnification of the electrochemically cycled cathode at discharged state. (d) High magnification of the electrochemically cycled cathode at discharged state.

crystallinity similar to that of the pristine cathode. This clearly indicates that the electrochemical lithiation and delithiation in the high Se content cathode are not damaging the lattice during the initial cycles, in contrast to the other chalcogen and oxide anion redox cathode materials.[13,42] The HRTEM image clearly demonstrates that a highly ordered structure is well maintained even in the case of a single Se substitution per formula unit ($Li_{1.13}Ti_{0.57}Fe_{0.3}S_1Se_1$).

Understanding of Anionic and Cationic Redox Activity through XAS. To further understand the redox participation of the elements, synchrotron XAS spectroscopy measurements of the S, Se, Ti, and Fe K-edges were carried out in cathode materials at different states of charge. In this work, it is expected that Li extraction is compensated by metal ion redox and anion redox reaction in the potential window of 1.8−3 vs Li/Li^+. Therefore, the anion redox participation was initially evidenced by surface-sensitive near edge X-ray absorption fine structure (NEXAFS) measurements. First, the NEXAFS measurement was carried out to analyze the Ti redox activity in the potential region used in this study. Here we will focus on two portions of the absorption spectra: (1) the pre-edge feature and (2) the main absorption edge peak. The pre-edge is sensitive toward the oxidation state and coordination environment of the absorbing atom being probed.[54] In this chalcogen composition, the Ti cation is in a tetravalent state with an octahedral coordination environment. The tetravalent Ti has empty $3d^0$ orbital (t_{2g}^0 e_g^0) configuration. Therefore, Ti oxidation beyond Ti^{4+} will not be possible during the Li extraction reaction because the *d* orbital

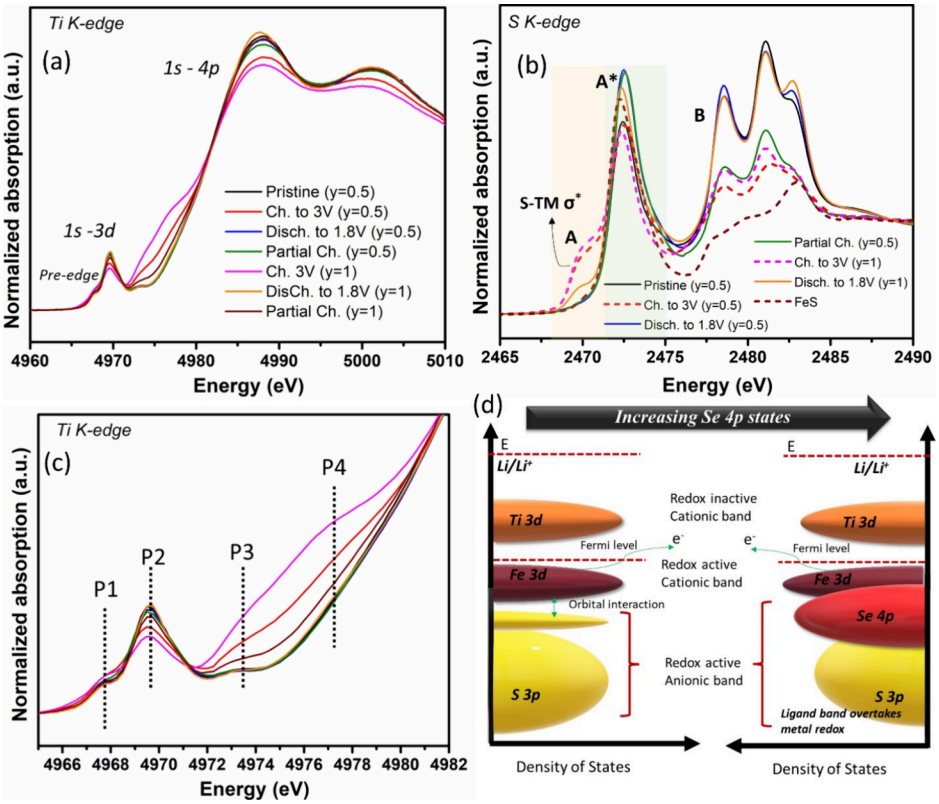

Figure 5. Near-edge X-ray absorption fine structure measurement of $Li_{1.13}Ti_{0.57}Fe_{0.3}S_{2-y}Se_y$ (y = 0.5 and 1). (a) Normalized Ti K-edge spectra; (b) normalized S K-edge spectra; (c) pre-edge spectra of Ti K-edge; (d) schematic representation of a Se-substituted chalcogen anion redox cathode. Based on the band position of Fe 3*d* band, initial Li extraction can be compensated by $Fe^{2+/3+}$ redox reaction followed by $Se^{2-/n-}$ redox and $S^{2-/n-}$ ($n < 2$) anionic redox reactions.

https://doi.org/10.1021/acs.chemmater.4c00854
Chem. Mater. 2024, 36, 8623−8638

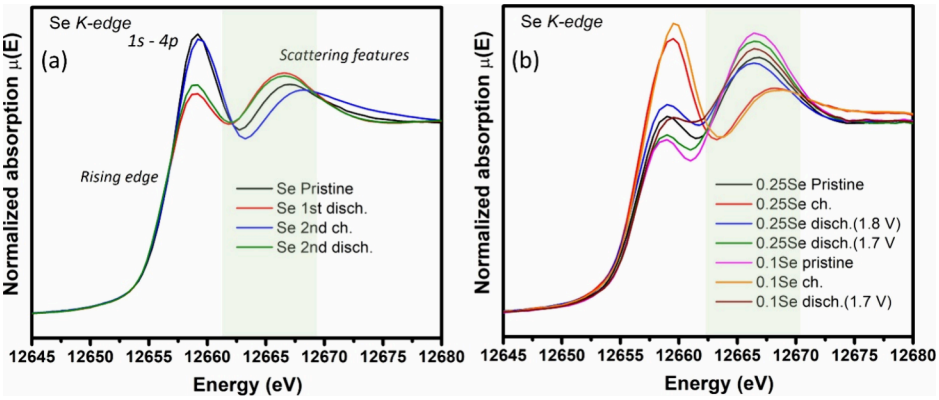

Figure 6. Hard X-ray absorption spectroscopy measurement of $Li_{1.13}Ti_{0.57}Fe_{0.3}S_{2-y}Se_y$. Se K-edge XANES spectra of (a) $y = 1$ and (b) $y = 0.25$ and 0.1.

has no electrons to compensate for Li extraction. The main absorption edge peak is ascribed to a transition of the 1*s* electron to the unoccupied 4*p* orbital.[55] To prove inactivity, the Ti K-edge NEXAFS measurements were evaluated (Figure 5a,c). Initially, the in-depth XAS analysis was conducted for $y = 0.5$ and extreme $y = 1$ Se cases to understand possible charge compensation mechanisms during different states of charge conditions. In both cathode compositions, when charging to 3 V, the Ti K-edge spectra exhibit notable changes in the line shape of the edge, which are due to the changes in the local environment of Ti during electrochemical reactions. However, the Ti K-edge spectra exhibit no rigid shifts at charged states, indicating that the Ti^{4+} cation is not taking part in the electron transfer reaction in the potential window of 1.8 to 3 V vs Li. However, there are significant changes in the pre-edge regions that are labeled P1−P4 in Figure 5c. A slight hump-like feature around 4968 eV, labeled as P1, corresponds to the quadrupole transition of 1*s*-to-3*d* states with t_{2g} symmetry coordinated in the octahedral environment of Ti cations. Next, the P2 peak indicates dipole-allowed transitions from Ti 1*s* to hybridized Ti 3*d*/4*p* orbital states.[56] Generally, the electric dipole transition is forbidden for 1*s* to 3*d* transition but allowed because of hybridized 3*d*/4*p* orbital states (*p* component rather than *d* component).[57] Interestingly, the P2 intensity is sensitive to orbital symmetry environments, and the intensity variation can be correlated to the displacement of Ti^{4+} cation in the Ti-$(S/Se)_6$ environment. There is a progressive decrement in the pre-edge intensity at different states of charge for the $y = 0.5$ and 1 Se compositions. Also, the P2 pre-edge intensity decreased to the minimum at a fully charged state for the high Se ($y = 1$ in $Li_{1.13}Ti_{0.57}Fe_{0.3}S_{2-y}Se_y$) composition, suggesting that anion oxidation during charge (S/Se) improves covalency between metal and chalcogen ligands that may be due to the shortening of Ti-Ch(S/Se) bond length (improved covalency).[31] The interaction between metal and ligand can lead to distortion in a high Se content $MS_{6-x}Se_x$ ($x \leq 6$) octahedral environment, confirming that the pre-edge intensity is decreased because of changes in the local octahedral symmetry. In addition, the other P3 and P4 peaks also substantiate this behavior, as high Se content composition shows significant line shape variations compared to $y = 0.5$ compositions in the fully charged state. The changes in the line shapes and pre-edge intensities are reversed during discharge, implying that the Se-substituted chalcogen anion redox reaction does not lead to any irreversible structural changes due to transition metal migration or parasitic redox couple evolutions. The metal migration and the redox couple evolutions are considered as detrimental challenges in Li-rich layered oxide cathodes.[13,16]

Further, the reversible anionic redox participation was evaluated using S K-edge spectra (Figure 5b). The involvement of anions (S^{2-}/Se^{2-}) in the redox participation was identified by observing significant changes in the spectral features of the S/Se K-edge spectra. The S K-edge spectra for different sample conditions with different Se substitutions and the $Fe^{2+}S^{2-}$ standard spectrum are shown in Figure 5b. The pristine composition exhibits a strong white line signal around 2470 eV that is comparable to previous S K-edge measurements of various alkali metal and transition metal sulfides.[58,59] It is known that metal 3*d* orbitals play a significant role in the pre-edge feature due to the hybridization between S 3*p* and metal 3*d* orbitals (M 3*d*−S 3*p*, σ^* antibonding orbitals). The hybridized states (denoted as A and A*) can be assigned to transitions from t_{2g} to e_g bandlike structures.[60] Because the initial Li extraction is expected to be compensated by transition metal redox, the oxidation of transition metal along with sulfur redox participation will improve the covalency between TM 3*d* and S 3*p* orbitals. However, for the fully charged state of both $y = 1$ and $y = 0.5$, a distinct shoulder peak emerged at low edge energy, and the shoulder is suppressed during the discharge state, implying that the S redox participation is reversible during electrochemical reactions. Also, the pristine state of $y = 0.5$ shows less main peak intensity compared to other charged states, suggesting that the synthesized pristine cathode ($y = 0.5$) may have a mixed valency of sulfur. This behavior strengthens the previous claim of the initial Li deficiency nature observed in the first cycle of electrochemical studies (see Figure 2c; the first charge is lower than discharge), suggesting that the Li deficiency nature may have influenced the valency of sulfur. When the cathode is charged to a partial state of charge (~50%), the pre-edge feature is not observed because of the limited amount of electron transfer from the S^{2-} anion, implying that the majority of the charge transfer is compensated by metal redox ($Fe^{2+/3+}$) at this stage. Fundamentally, when anions have participated in redox reactions, anion oxidation reactions increase electron holes on the anions, and the increase in electron holes could be reflected as a hump/shoulder in the S K-edge spectra at high states of charge conditions.[58,61−63] As per S K-edge spectra, when the electrons are released upon Li extraction, the S^{2-} anion is oxidized (S^{n-},wherein $n < 2$), and the electron holes are created on top of S 3*p* band. Further, the electron holes from sulfur are stable, and thus, a distinct shoulder peak is

https://doi.org/10.1021/acs.chemmater.4c00854
Chem. Mater. 2024, 36, 8623−8638

observed in the S K-edge spectra when the S^{2-} anion attains a high valence state compared to that of pristine. In addition, the origin of the single S K-edge peak around 2470 eV is mainly from the electron hole character without any noticeable S−S dimer formation.[64] This observation proves that the strong metal ligand covalency character can stabilize the holes during the electrochemical process for reversible redox reactions. The peaks after 2472 eV (denoted as B) are mainly responsible for the hybridized S 3*p* states with M 4*s*/4*p* unoccupied bands. With this understanding, we confirm that the shoulder peak was observed reversibly during the electrochemical reaction of the cathode, and this behavior is attributed to the reversible sulfide anion redox nature in these cathodes with different Se content. A pictorial representation of the Se 4*p* redox couple pinning process in the sulfide framework, leading to improved metal ligand covalency influencing anion redox reversibility, is shown in Figure 5d.

Bulk Redox Activity of Anion and Cation Redox Couples (Se and Fe K-Edges). After gaining insights into the redox species through NEXAFS investigations, we further delved into the redox contribution of Se species using hard X-ray absorption spectroscopy (XAS). This allowed us to identify variations in the redox state and changes in the local coordination environment resulting from covalent interactions between metal−ligand bonding during Se anion redox reactions (Figure 6). As shown in Figure 6a, the Se K-edge spectra for $Li_{1.13}Ti_{0.57}Fe_{0.3}S_1Se_1$ exhibit a few important spectral features; mainly the white line intensity, arising from 1*s* to 4*p* unoccupied energy transition, varied with both the Se valence state variation and bonding environment changes.[65] There are two spectral features observed: (i) white line intensity variation at 12657 eV and (ii) near-edge peak intensity variations. The intensity variation associated with the white line is mainly attributed to the Se valence state during the Se redox contribution. This white line intensity was previously correlated to identify Se valence states in various Se-based compositions such as Se (VI), Se (II), and Se^0.[66] Fundamentally, the white line gains intensity as valency decreases (Se^{2-} to Se^{n-}, $n < 2$), which is directly attributable to an increase in the population of the 4*p* valence levels.[34] Similarly, a feature observed at 12,665.5 eV has a strong correlation to its local environment, and Se anion oxidation significantly reduced the intensity and shifted the spectrum to a high-energy region. With these spectral features, the Se redox contribution was confirmed in Se-substituted compositions (Figure 6a). First, the high Se content composition ($y = 1$) was evaluated where the pristine compositions exhibit an increased white line intensity, and a scattering feature was observed between the fully charged and discharged conditions. This behavior may be attributed to the mixed valence states of Se species from either the solid-state synthesis or the presence of Se species from the pristine composition. In addition, at a fully charged state, the white line intensity was increased, and a scattering feature at 12,665 eV is shifted to high energy that clearly indicates the oxidation of Se species. This observation was later supported with the theoretical Se K-edge spectral simulation for a representative composition (Figure 7). However, after the first cycle discharged state, the white line intensity is reduced, and the scattering feature is shifted back to low energy, indicating that the oxidized Se anion is reversed to lower valence state, especially Se^{n-} ($n < 2$) to Se^{2-}. A similar feature was replicated in the second discharged state of $Li_{1.13}Ti_{0.57}Fe_{0.3}S_1Se_1$, indicating the complete reversibility of

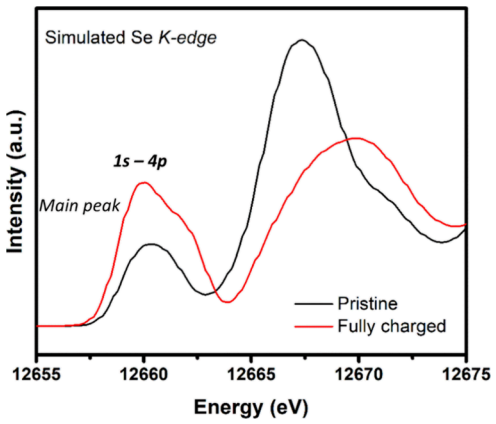

Figure 7. Simulated Se K-edge X-ray absorption spectra of a representative structure (see text for further details) before and after delithiation.

the Se electronic structure and local environment during Se anion redox contribution. Further, the XAS spectroscopy investigations were extended to analyze lower Se content compositions ($y = 0.25$ and 0.1) that are electrochemically superior to other Se-substituted compositions (Figure 6b). Similar to $Li_{1.13}Ti_{0.57}Fe_{0.3}S_1Se_1$, the Se K-edge spectra of $y = 0.25$ and $y = 0.1$ Se-substituted compositions look similar, and no additional spectral features were observed compared to the high Se content composition. This observation once again confirms that the Se substitution has not significantly modified the local environment. Two different Se compositions were investigated for different state of charge conditions: pristine, charged to 3 V, and discharged to 1.8 and 1.7 V vs Li. After understanding the electrochemical importance of lower Se compositions, the discharge voltage of the Se composition was slightly lowered from 1.8 to 1.7 V because the slight extension in discharge voltage may lead to a significant change in local environment as proven previously in $Li_2TiS_{1.5}Se_{1.5}$ composition.[35] The Se K-edge spectrum of the pristine composition exhibits similar features except for a slight intensity variation between the two compositions. Compared to $y = 0.25$ Se, the $y = 0.1$ Se composition main peak intensity reaches slightly higher, and a scattering feature around 12,665 eV is also shifted to high energy. The observed behavior may be attributed to the significant contribution of Se species because less Se content in the composition may have the possibility to complete Se utilization to achieve targeted 1 Li transfer electrochemical reactions. Conversely, more Se content in the composition technically reduces the gravimetric capacity of the composition due to the heavier mass of Se compared to the S ligand, and the available Se contribution toward achieving 1 Li transfer may not need whole Se content compared to S^{2-}/S^{n-} ($n < 2$) and $Fe^{2+/3+}$ redox contribution in the overall composition. Although similar features are observed, the relative intensity between the main absorption peak and the high energy scattering feature is not of the same magnitude. At the fully discharged state, lower Se content ($y = 0.1$ and 0.25) compositions exhibited high intensity scattering features compared to high Se content compositions. This observation can be correlated with the previous explanation focusing on the relation between Se content and the demand for Se redox contribution in comparison with high Se content. Se and S K-edge redox contributions were further supported with

https://doi.org/10.1021/acs.chemmater.4c00854
Chem. Mater. 2024, 36, 8623−8638

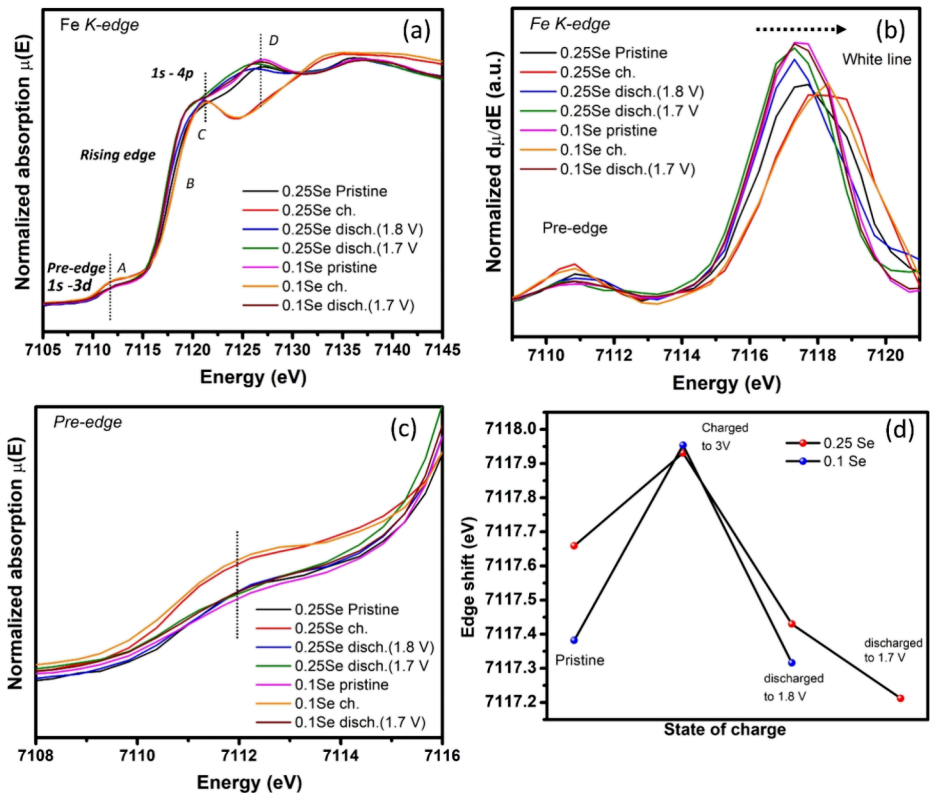

Figure 8. Hard X-ray absorption spectroscopy of $Li_{1.13}Ti_{0.57}Fe_{0.3}S_{2-y}Se_y$ (y = 0.25, 0.1). (a) Fe K-edge spectra, (b) first derivative Fe K-edge spectra, (c) pre-edge region of the Fe K-edge XANES spectra, and (d) edge shift of Fe K-edge spectra. Edge shift was measured based on the half height method.

HAXPES measurements, and a detailed explanation (S 1*s* and Se 2*p* spectra) is given in Supporting Note 3.

In addition, the Se K-edge behavior after delithiation was supported by computationally simulated spectra. This simulation involved core-exciting a representative Se atom from the composition $Li_{1.11}Ti_{0.55}Fe_{0.33}S_{1.78}Se_{0.22}$, which is in close agreement with the experimentally observed composition $Li_{1.13}Ti_{0.57}Fe_{0.3}S_{1.75}Se_{0.25}$. Details of the computational method used for the simulation are included in the Supporting Information. Figure 7 shows that the simulated spectra for the pristine ($Li_{1.11}Ti_{0.55}Fe_{0.33}S_{1.78}Se_{0.22}$) and the fully charged (i.e., delithiated) system reproduce the two main features of their experimental counterparts at about 12,657 and 12,665 eV, as well as the energy separation (~7 eV, scattering peak ~0.2 eV shifted after charge) between the peaks. In addition, the relative intensity of the pristine composition is reproduced with a slight underestimation of the spectrum for the fully charged state. Most importantly, the simulated spectra qualitatively replicate the experimental observation (Figure 6b) that the first peak of the fully charged spectrum is noticeably more intense than the pristine one. This suggests that the Se orbitals indeed take part in the redox reaction during Li extraction. Fundamentally, we hypothesize that the involvement of the Se contribution to the 1 Li transfer reaction is relatively high in lower Se composition. Considering the redox-active Fe-(S/Se) octahedral regions, both the Fe^{2+}/Fe^{3+} cation redox and the S^{2-}/Se^{n-} (where $n < 2$) anion redox processes are highly likely to alter the Se bonding environment significantly. The interaction between the metal and ligand during combined cationic and anionic redox processes will undoubtedly influence the spectral features of individual species, particularly leveraging the advantages of metal−ligand covalency.

Cationic Redox Contribution at Different State of Charge. Having gained a better understanding of anion redox, we proceeded to analyze the electrochemically important compositions for the cation redox contribution. This was achieved through Fe K-edge spectroscopy investigations (Figure 8). The general features of the Fe K-edge consist of low energy pre-edge, rising edge, K-edge main peak, and high energy photoemission scattering peaks. The observed Fe K-edge spectra of the Se-substituted cathode materials look like iron chalcogenides (Li_2FeS_2, FeS_2, FeSe, $FeSe_2$) previously reported for both octahedral and tetrahedral coordinations.[32,67,68] Similarly, the Fe K-edge spectrum was marked with the following identified features: pre-edge A, rising edge B, K-edge C, and high-energy scattering feature D. First, the pre-edge peak at 7112 is due to the 1*s*-to-3*d* transition through a weak quadrupole transition. The strength as well as the intensity of the pre-edge peak is strongly influenced by the coordination environment, local geometry, or distortion associated with the absorbing atomic environment. The rising edge is due to the absorption edge jump that is mainly ascribed to the 1*s*-to-4*p* transition. Further, the main absorption edge is due to the transition from the 1*s*-to-4*p* state admixed with the *d* states from the chalcogen (S/Se) atoms. Finally, the high energy peak features are due to the photoemission scattering process with the near neighbors.[68] As shown in Figure 8a, the pre-edge intensity is not strong or intense for all the state of charge conditions compared to other tetrahedral Fe-Ch(S/Se) environments in the existing literature.[32,67] Fundamentally, electric dipole transitions are allowed through *p*-*d* hybrid-

https://doi.org/10.1021/acs.chemmater.4c00854
Chem. Mater. 2024, 36, 8623−8638

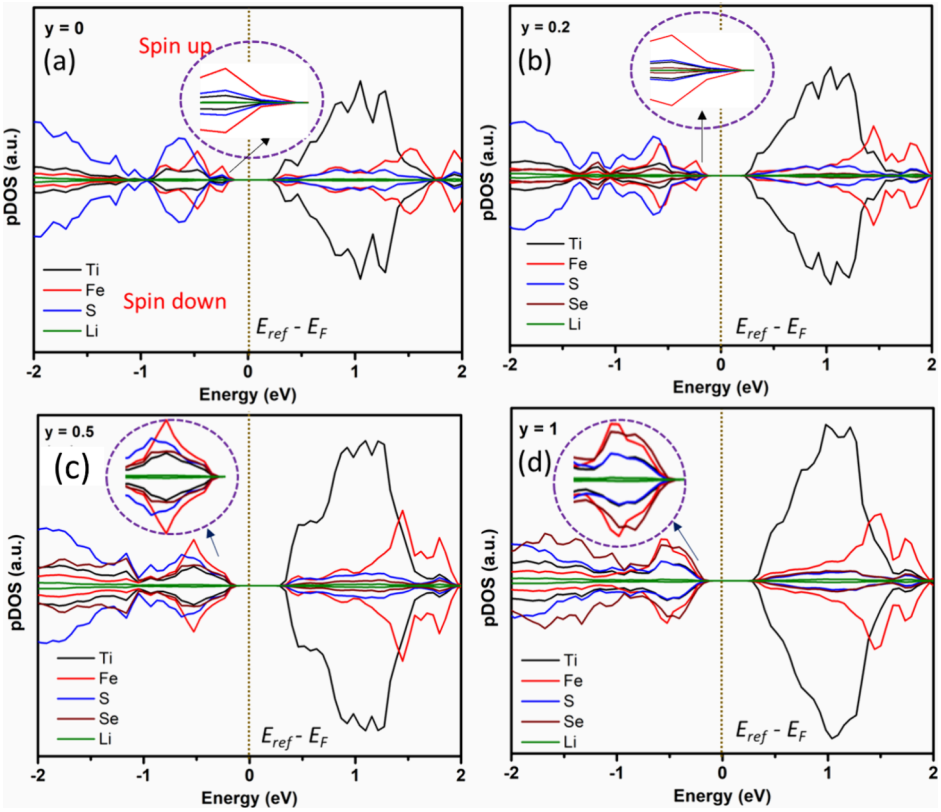

Figure 9. Projected density of states of $Li_{1.11}Ti_{0.55}Fe_{0.33}S_{2-y}Se_y$ (y = 0, 0.22, 0.55, and 1) cathodes. (a) y = 0, (b) y = 0.22, (c) y = 0.55, and (d) y = 1. All calculations were performed with the GGA+U functional with antiferromagnetic configuration (methods).

ization in tetrahedral geometry, but the octahedral geometry can proceed through electric quadrupole transitions that are much less intense than the dipole transitions.[69] In the chalcogen framework, the Fe atom is coordinated with six ligands in an octahedral coordination. In addition, the Fe-*X* (*X:* S/Se) environment is more covalent than the metal−oxygen environment, so the covalent interaction supports the less pre-edge intensity. By carefully looking at the pre-edge features (Figure 8c), the pristine and discharged state conditions exhibit only minimal changes in the spectral features, but the charged states exhibit slightly higher intensity than the other conditions. At the fully charged state, the observed behavior is due to a higher degree of covalency that resulted from the mixed cation/anion redox reactions. In this Fe-X_6 (*X*: S/Se) octahedral geometry, when fully charged, the Fe and chalcogen (S/Se) are involved in redox reactions that could increase the covalency between the metal and ligand, leading to distortion in the original octahedral geometry as shown in scattering features of the Fe K-edge. Therefore, the pre-edge features indicate reversible $Fe^{2+/3+}$ redox and covalent interactions between metal (Fe) and chalcogen (S and Se) ligands during electrochemical redox reactions. Next, the rising edge energy is attributed to the oxidation state of the absorbing atom. The edge energy shift is well visualized in the first derivative of the Fe K-edge spectra (Figure 8b). In general, the absorption edge is determined by the first inflection point in the derivative spectrum or half of the spectrum. During the fully charged state, the first derivative of the y = 0, 0.25, and 0.1 compositions shifted from 7117 to 7118.5 eV because of Fe^{2+} oxidation changes to a higher oxidation state (Figure 8d). The shift in the rising edge and the first derivative peak around 7117 eV reversed back to lower E_o edge energy upon discharge, indicating that the Fe cationic redox reaction is reversibly occurring during electrochemical charge−discharge reactions. Further, the main peak intensity is slightly decreased in height, and also the peak shape changed to intense upon charging, which is clearly observed in Fe K-edge XANES spectra and first derivative spectra of the Fe K-edge spectra. This phenomenon is mainly due to the large mixing of Fe *d*-*X* (*X:* S/Se) *p* states, resulting in high S/Se degree of covalency when utilizing cationic and anionic redox at high state of charge. There is no significant deviation in y = 0.25 and y = 0.1 Se-substituted compositions, but the magnitudes of the energy shifts are almost similar during charge and discharge. Additionally, compositions with y = 0.25 and y = 0.1 were discharged to 1.7 V to identify any significant spectroscopic changes. Interestingly, the lower cutoff voltage of 1.7 V has no effect on the spectral features of the Se-substituted compositions (y = 0.25 and y = 0.1), indicating that the Fe valence state variation in the 0.1 V difference is negligible. Finally, the high energy features exhibited minor changes at fully charged and discharged states, confirming highly reversible spectroscopic evidence of Fe redox contribution. More importantly, the observed electrochemical behavior of the Se-substituted cathodes is contrary to the existing Se-substituted composition in Li_2FeS_2 cathodes. The Se substitution in Li_2FeS_2 resulted in a huge capacity fade, with over 80% of the initial capacity lost within 100 charge−discharge cycles at C/10 current rate.[34] Also, sulfide compositions in other structural motifs such as antiperovskite and layered sodium cathodes exhibited relatively less cycling stability, and all are majorly limited to only 100 cycles with greater capacity decay.[30,70] However, in our work, the Se substitution yields additional stability and rate capability in the

https://doi.org/10.1021/acs.chemmater.4c00854
Chem. Mater. 2024, 36, 8623−8638

sulfide framework and compensates for partial charge contribution for achieving highly reversible (10C charge rate) Se-substituted chalcogen cathode materials free from Ni and Co metals.

DFT-Based Electronic Structure Calculation. To substantiate the experimental observation, spin-polarized DFT calculations were performed on the different Se-substituted compositions $Li_{1.11}Ti_{0.55}Fe_{0.33}S_{2-y}Se_y$ (y = 0, 0.22, 0.55, and 1). The structure models were manually constructed from rhombohedral $LiTiS_2$ (R-3m) to obtain the Li_2TiS_3 system. Further, Li and Ti atoms were replaced with an appropriate number of Fe atoms to achieve a composition of $Li_{1.11}Ti_{0.55}Fe_{0.33}S_{2-y}Se_y$ (y = 0, 0.22, 0.55, and 1), which is in close approximation with the experimental compositions $Li_{1.13}Ti_{0.57}Fe_{0.3}S_{2-y}Se_y$ (0, 0.1, 0.2, 0.5, and 1). To construct Se-substituted models, S atoms in the pristine composition were replaced with Se atoms to get approximately 0.22, 0.55, and 1 Se per formula unit. The compositions are chosen for computational convenience. The constructed models with both experimental and theoretical compositions are shown in Figure S15. With the pristine and Se-substituted structures, geometry relaxations and projected density of states (pDOS) calculations with spin-polarized calculations were performed. As shown in Figure 9, the calculated pDOS plots of different compositions reveal that the S, Se, and Fe states are dominating the occupied bands below the Fermi level, whereas the dominant Ti 3d states are lying above the Fermi level (E_F). It was found that the antiferromagnetic (AFM) structure had a low energy, with an energy difference of approximately 0.26 eV compared to the ferromagnetic (FM) model. The AFM configuration is shown in Figure 9, whereas the FM configuration is shown in Figure S12. In the y = 0 structure, spin-down Fe 3d states and spin-up S 3p states equally dominated in the vicinity of the Fermi level, indicating the hybridized states of Fe−S bonds. Also, the states near the Fermi level contribute to the electrochemical redox activity by involving electron transfer reactions during Li extraction. When gradually increasing Se content, the states near the Fermi level changed, confirming the Se contribution to the electronic structure of the cathode materials. Because of less electronegativity of Se, the covalent interaction between transition metal 3d and Se 4p ligand is higher than the metal 3d−S 3p interaction.

As shown in Figure 9, the Se 4p states emerges in the vicinity of the Fermi level as the Se content increases. However, in the 0.22 Se structure, S 3p and Fe 3d states still dominate at the valence band edge. Therefore, it is evident that Fe 3d and S 3p are the dominant charge contributors during Li insertion and extraction compared to Se 4p states in the low Se content compositions ($y \leq 0.5$). This theoretical observation supported our experimental electrochemistry results that the Fe cationic redox ($Fe^{2+/3+}$) region in the initial delithiation fades slowly with an increasing Se content (Figure 2). This observation was also supported by cyclic voltammetry investigation of different Se content compositions, where the cationic redox peaks fade as Se content increases (Figure S10). Furthermore, the structure with 1 Se per formula unit exhibits a valence band region dominated by Se 4p states compared to S 3p and Fe 3d states in the vicinity of the Fermi level. In the case of $Li_{1.13}Ti_{0.57}Fe_{0.3}S_1Se_1$ (1 Se per f.u.), Se 4p states are lying above the S 3p and Fe 3d states, leading to easily taking part in the charge contribution during Li extraction reactions. This observation confirms that the initial charge compensation mainly originates from Se anion redox reactions. For 1 Se per formula unit, half of the sulfur atoms in the supercell were completely replaced with Se atoms. This observation supports the electrochemical investigation in which the high Se-substituted cathode shows less Fe redox region during charging and discharging, implying that the Li-ion extraction is primarily dominated by possibly mixed chalcogen anion redox contribution (S/Se). Based on the theoretical capacity calculation, the high Se structures dominated most of the capacity from Se anionic redox followed by S anion redox. Also, the maximum amount of capacity from the $Fe^{2+/3+}$ redox gets reduced when Se content is increased. Overall, this theoretical investigation of different Se substituted structures confirms the possible charge contributors and their preferential redox activity during Li extraction. Further, as shown in XRD, adding Se into sulfide framework increases the c-axis lattice parameter as this behavior was confirmed with the shifting of Bragg peaks moving toward lower angles (Figure 1b). In theory, the optimized geometries of lithiated structures unequivocally validate that the c-axis lattice parameter increases proportionally with the increase of Se content (Figure S13). The observed lattice expansion is in excellent agreement with our experimental findings (Figure 1). Furthermore, this lattice expansion may contribute to the enhanced high-rate capability observed in cathodes with a high Se content due to efficient Li transport in the Li layer.[46] Therefore, we explored how Se substitution improves the metal−ligand interaction in this work. Figure S14 shows the net Bader charge of S/Se atoms as a function of lithium content for different Se content compositions $Li_{1.11}Ti_{0.55}Fe_{0.33}S_{2-y}Se_y$ (y = 0 and 1). It is clearly seen that the Se atoms are preferentially oxidized when all layered Li atoms are removed. This similar behavior was observed in pDOS of the high Se content composition (y = 1). Interestingly, the ferromagnetic structure also exhibited a similar behavior near the Fermi level, with the Se 4p states becoming more prominent at the valence band maximum (Figure S12). Additionally, the spin-down channels of the Fe d states shifted to lower energy levels, resulting from the dominant Se 4p states occupying positions near the Fermi level. This observation once again corroborates that cathodes with a high Se content preferentially can release electrons through redox reactions during electrochemical Li extraction.

Influence of Se 4p States on VB Spectra. To further substantiate the influence of Se on electronic structure, valence band spectra were measured with the HAXPES technique. High photon energy (3100 eV) was used to probe the bulk of the materials. As shown in Figure 10, the VB spectra based on the HAXPES technique display the electron density of the occupied states near the Fermi level. A close observation of the VB spectra reveals that the Se substitution leads to shifting of the valence band maximum (VBM) toward the Fermi level, indicating that the Se 4p states are dominating near the Fermi level. The valence band edge (E_v) values were obtained by the intersection of the extrapolated line from the base and linear portion of the VB spectra near the Fermi level. The VBM values are 1.9, 1.65, and 1.4 eV for 0, 0.5, and 1 Se, respectively. Also, it is possible that the Se addition in atomic level can modify the band gap of the materials as Se possesses slightly lower electronegativity than sulfur, leading to enhanced covalency. Therefore, the Se substitution in the sulfide framework modified the electronic structure and redox activity of the materials to achieve improved kinetics.

https://doi.org/10.1021/acs.chemmater.4c00854
Chem. Mater. 2024, 36, 8623−8638

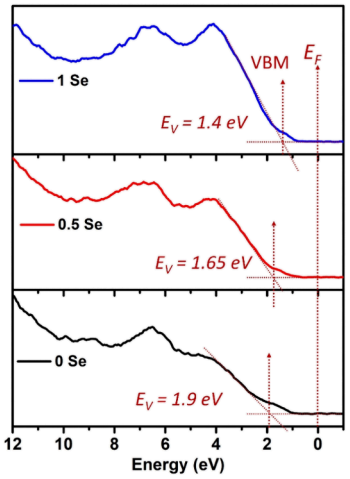

Figure 10. HAXPES VB spectra of $Li_{1.13}Ti_{0.57}Fe_{0.33}S_{2-y}Se_y$ (y = 0, 0.5, and 1) cathodes (E_F: Fermi level, VBM: valence band maximum, E_V: valence band edge).

CONCLUSIONS

In this work, a Ni- and Co-free fast charging cathode was investigated through leveraging multianion chalcogen redox in the model structural framework ($Li_{1.13}Ti_{0.57}Fe_{0.3}S_{2-y}Se_y$) by appropriate tuning of metal−ligand covalency with less electronegative and softer anion of Se atoms. A systematic shift in Bragg peaks confirmed the Se mixing in the lattice and its associated lattice expansion. The effect of the Se 4*p* band on the electrochemical reversibility involving multicomponent redox ($Fe^{2+/3+}$, S^{2-}/S^{n-}, Se^{2-}/Se^{n-}, wherein $n < 2$) in the Li-rich chalcogen environment affected the electronic structure of the cathode and its electrochemical properties, such as average redox voltage, anion redox reversibility, and rate capability. Further, highly covalent metal−ligand interactions in the chalcogen framework led to deliver high reversibility at C/2 rate even after high-rate (1C) charge−discharge reactions. Interestingly, the chalcogen framework (y = 0.25) exhibited high-rate capability at more than 10C (~6 min charge) charge−discharge rate, delivering more than 50% of the capacity (~120 mAh/g) obtained at C/20 rate (220 mAh/g). A systematic shift in average redox voltage (~2.5 to 2.3 V vs Li) during electrochemical reaction was observed at different Se substitutions due to changes in the metal−ligand covalency or band positions. Further, the in-depth XAS investigation revealed that the spectral features of Fe, S, and Se K-edge are highly reversible, and all three elements contributed to electron transfer reactions in the potential region of the study (1.8 vs 3 V vs Li). Sulfur K-edge measurements revealed that the majority electron transfer is dominated by S^{2-}/S^{n-} ($n < 2$) reaction through hole stabilization on S 3*p* bands during electrochemical charging. In contrast to previous works, the Se addition in the chalcogen framework improved anion redox reversibility, and also, the Ti^{4+} cation environment in the cathode was not distorted to activate Ti redox. Throughout the charge/discharge reaction, the Ti^{4+} [$3d^0$ (t_{2g}^0 e_g^0)] remains as a buffer cation, and its redox inactivity was deduced from the Ti K-edge spectra lacking any noticeable energy shifts. In addition, probing of S 1*s* and Se 2*p* core lines at 3100 eV using HAXPES confirmed the reversible spectral variations of S−S/S−Se peak contributions, indicating the involvement of ligands in highly reversible electrochemical anion redox reactions. The DFT calculations strongly supported the experimental observations including the lattice expansion behavior, Se K-edge spectroscopy features, and metal−ligand electronic contribution toward electrochemical properties. The pDOS measurements ensured the population of ligand *p* orbitals (S 3*p* and Se 4*p*) along with Fe 3*d* states in the vicinity of the Fermi level, indicating the highly hybridized states of Fe-*X* (*X*: S, Se) bonds responsible for electron transfer reactions. When introducing higher Se content in the lattice (50% Se per f.u. or $Li_{1.13}Ti_{0.57}Fe_{0.3}S_1Se_1$), the valence band edge is dominated by Se 4*p* states near the Fermi level, identified through HAXPES-based VB spectra and DFT calculations. This fundamental interplay between the metal−ligand interactions in chalcogen family cathodes is the reason for the improved kinetics and electrochemical property of the anion redox cathodes. The observed findings can lead to the identification of electrochemically superior compositions for developing high-capacity and high-rate anion redox cathodes.

ASSOCIATED CONTENT

Supporting Information

The Supporting Information is available free of charge at https://pubs.acs.org/doi/10.1021/acs.chemmater.4c00854.

Images of the quartz ampule and capillary; EDAX images of y = 0.5 and 1 Se cathodes; (dQ/dV) plot for all compositions; voltage profiles (cycle nos. 1 and 3) of all compositions; theoretical capacity table; GITT analysis; S 1*s* and Se 2*p* HAXPES spectra of y = 0.5 Se composition; CV profiles of all compositions (y = 0.1, 0.25, 0.5, and 1); rate performance and cycle stability of compositions (y = 0, 0.1, and 0.25); projected density of state plots of all compositions (y = 0, 0.2, 0.5, and 1); *c*-axis lattice parameter vs Se content per f.u. plot; Bader charge plot; and structure models for the DFT calculations (PDF)

AUTHOR INFORMATION

Corresponding Author

Leela Mohana Reddy Arava − *Department of Mechanical Engineering, Wayne State University, Detroit, Michigan 40202, United States;* orcid.org/0000-0001-6685-6061; Email: leela.arava@wayne.edu

Authors

Sudhan Nagarajan − *Department of Mechanical Engineering, Wayne State University, Detroit, Michigan 40202, United States;* orcid.org/0000-0002-3524-5062

Subhayan Roychoudhury − *The Molecular Foundry, Lawrence Berkeley National Laboratory, Berkeley, California 94720, United States;* orcid.org/0000-0003-1426-2039

Conan Weiland − *Material Measurement Laboratory, National Institute of Standards and Technology, Gaithersburg, Maryland 20899, United States*

Debora Motta Meira − *Canadian Light Source, Saskatoon, Saskatchewan S7N 2 V3, Canada;* orcid.org/0000-0002-7529-2736

Mahalingam Balasubramanian − *X-ray Science Division, Advanced Photon Source, Argonne National Laboratory, Lemont, Illinois 60439, United States;* Present Address: Present address: Electrification and Energy Infrastructure Division, Oak Ridge National Laboratory, Oak Ridge, Tennessee 37830, United States; orcid.org/0000-0002-3988-3125

https://doi.org/10.1021/acs.chemmater.4c00854
Chem. Mater. 2024, 36, 8623−8638

David Prendergast − *The Molecular Foundry, Lawrence Berkeley National Laboratory, Berkeley, California 94720, United States;* orcid.org/0000-0003-0598-1453

Sooyeon Hwang − *Center for Functional Nanomaterials, Brookhaven National Laboratory, Upton, New York 11973, United States;* orcid.org/0000-0001-5606-6728

Complete contact information is available at: https://pubs.acs.org/10.1021/acs.chemmater.4c00854

Notes

The authors declare the following competing financial interest(s): S.N. and L.M.R.A. report a U.S. provisional patent application relevant to this research (Serial No. 63/459,797), filed on April 17, 2023, followed by subsequent U.S. non-provisional and PCT applications filed on April 17, 2024.

■ ACKNOWLEDGMENTS

This work was primarily supported by the National Science Foundation under grant number 2127519. This research used resources of the National Synchrotron Light Source II (NSLS-II), a U.S. Department of Energy (DOE) Office of Science User Facility operated for the DOE Office of Science by Brookhaven National Laboratory under Contract DE-SC0012704. The HAXPES and NEXAFS measurements were performed at the National Institute of Standards and Technology (NIST) beamline SST-2 in the NSLS-II. This research also used resources of the Center for Functional Nanomaterials, which is a U.S. DOE Office of Science Facility, at Brookhaven National Laboratory under Contract DE-SC0012704. This research used resources of the Advanced Photon Source, an Office of Science User Facility operated for the U.S. Department of Energy (DOE) Office of Science by Argonne National Laboratory, and was supported by the U.S. DOE under Contract DE-AC02-06CH11357 and the Canadian Light Source and its funding partners. The theoretical analysis in this work was supported by a User Project at The Molecular Foundry and its computing resources, managed by the High-Performance Computing Services Group at Lawrence Berkeley National Laboratory (LBNL). This research also used resources of the National Energy Research Scientific Computing Center (NERSC), a U.S. Department of Energy Office of Science User Facility located at LBNL. The LBNL facilities employed in this work were supported by the Director, Office of Science, Office of Basic Energy Sciences of the United States Department of Energy under Contract DE-AC02-05CH11231. This work used resources of the Lumigen Instrument Center at Wayne State University for the use of XRD (NSF: MRI 1427926) facility.

■ REFERENCES

(1) Cai, Z.; Ouyang, B.; Hau, H.-M.; Chen, T.; Giovine, R.; Koirala, K. P.; Li, L.; Ji, H.; Ha, Y.; Sun, Y.; Huang, J.; Chen, Y.; Wu, V.; Yang, W.; Wang, C.; Clément, R. J.; Lun, Z.; Ceder, G. In situ formed partially disordered phases as earth-abundant Mn-rich cathode materials. *Nature Energy* **2024**, *9* (1), 27−36.

(2) Huang, J.; Ouyang, B.; Zhang, Y.; Yin, L.; Kwon, D.-H.; Cai, Z.; Lun, Z.; Zeng, G.; Balasubramanian, M.; Ceder, G. Inhibiting collective cation migration in Li-rich cathode materials as a strategy to mitigate voltage hysteresis. *Nat. Mater.* **2023**, *22* (3), 353−361.

(3) Goodenough, J. B.; Park, K.-S. The Li-Ion Rechargeable Battery: A Perspective. *J. Am. Chem. Soc.* **2013**, *135* (4), 1167−1176.

(4) Goodenough, J. B.; Kim, Y. Challenges for Rechargeable Li Batteries. *Chem. Mater.* **2010**, *22* (3), 587−603.

(5) Li, B.; Tarascon, J.-M., Status of Li(Na)-based anionic redox materials for better batteries. In *Comprehensive Inorganic Chemistry III (Third ed.)*; Elsevier: Oxford, 2023, 6−45.

(6) Rozier, P.; Tarascon, J. M. Review—Li-Rich Layered Oxide Cathodes for Next-Generation Li-Ion Batteries: Chances and Challenges. *J. Electrochem. Soc.* **2015**, *162* (14), A2490−A2499.

(7) Gent, W. E.; Busse, G. M.; House, K. Z. The predicted persistence of cobalt in lithium-ion batteries. *Nature Energy* **2022**, *7* (12), 1132−1143.

(8) Zhang, R.; Wang, C.; Zou, P.; Lin, R.; Ma, L.; Li, T.; Hwang, I.-h.; Xu, W.; Sun, C.; Trask, S.; Xin, H. L. Long-life lithium-ion batteries realized by low-Ni, Co-free cathode chemistry. *Nature Energy* **2023**, *8* (7), 695−702.

(9) Liu, T.; Yu, L.; Liu, J.; Lu, J.; Bi, X.; Dai, A.; Li, M.; Li, M.; Hu, Z.; Ma, L.; Luo, D.; Zheng, J.; Wu, T.; Ren, Y.; Wen, J.; Pan, F.; Amine, K. Understanding Co roles towards developing Co-free Ni-rich cathodes for rechargeable batteries. *Nature Energy* **2021**, *6* (3), 277−286.

(10) Li, B.; Zhuo, Z.; Zhang, L.; Iadecola, A.; Gao, X.; Guo, J.; Yang, W.; Morozov, A. V.; Abakumov, A. M.; Tarascon, J.-M. Decoupling the roles of Ni and Co in anionic redox activity of Li-rich NMC cathodes. *Nat. Mater.* **2023**, *22* (11), 1370−1379.

(11) Croy, J. R.; Balasubramanian, M.; Gallagher, K. G.; Burrell, A. K. Review of the US Department of Energy's "Deep Dive" effort to understand voltage fade in Li-and Mn-rich cathodes. *Accounts of chemical research* **2015**, *48* (11), 2813−2821.

(12) Assat, G.; Tarascon, J.-M. Fundamental understanding and practical challenges of anionic redox activity in Li-ion batteries. *Nature Energy* **2018**, *3* (5), 373−386.

(13) Hu, E.; Yu, X.; Lin, R.; Bi, X.; Lu, J.; Bak, S.; Nam, K.-W.; Xin, H. L.; Jaye, C.; Fischer, D. A.; Amine, K.; Yang, X.-Q. Evolution of redox couples in Li- and Mn-rich cathode materials and mitigation of voltage fade by reducing oxygen release. *Nat. Energy* **2018**, *3* (8), 690−698.

(14) Hong, J.; Gent, W. E.; Xiao, P.; Lim, K.; Seo, D.-H.; Wu, J.; Csernica, P. M.; Takacs, C. J.; Nordlund, D.; Sun, C.-J.; Stone, K. H.; Passarello, D.; Yang, W.; Prendergast, D.; Ceder, G.; Toney, M. F.; Chueh, W. C. Metal−oxygen decoordination stabilizes anion redox in Li-rich oxides. *Nat. Mater.* **2019**, *18* (3), 256−265.

(15) Gent, W. E.; Lim, K.; Liang, Y.; Li, Q.; Barnes, T.; Ahn, S.-J.; Stone, K. H.; McIntire, M.; Hong, J.; Song, J. H.; Li, Y.; Mehta, A.; Ermon, S.; Tyliszczak, T.; Kilcoyne, D.; Vine, D.; Park, J.-H.; Doo, S.-K.; Toney, M. F.; Yang, W.; Prendergast, D.; Chueh, W. C. Coupling between oxygen redox and cation migration explains unusual electrochemistry in lithium-rich layered oxides. *Nat. Commun.* **2017**, *8* (1), 2091.

(16) Eum, D.; Kim, B.; Kim, S. J.; Park, H.; Wu, J.; Cho, S.-P.; Yoon, G.; Lee, M. H.; Jung, S.-K.; Yang, W.; Seong, W. M.; Ku, K.; Tamwattana, O.; Park, S. K.; Hwang, I.; Kang, K. Voltage decay and redox asymmetry mitigation by reversible cation migration in lithium-rich layered oxide electrodes. *Nat. Mater.* **2020**, *19* (4), 419−427.

(17) House, R. A.; Rees, G. J.; Pérez-Osorio, M. A.; Marie, J.-J.; Boivin, E.; Robertson, A. W.; Nag, A.; Garcia-Fernandez, M.; Zhou, K.-J.; Bruce, P. G. First-cycle voltage hysteresis in Li-rich 3d cathodes associated with molecular O2 trapped in the bulk. *Nature Energy* **2020**, *5* (10), 777−785.

(18) Luo, K.; Roberts, M. R.; Hao, R.; Guerrini, N.; Pickup, D. M.; Liu, Y.-S.; Edström, K.; Guo, J.; Chadwick, A. V.; Duda, L. C.; Bruce, P. G. Charge-compensation in 3d-transition-metal-oxide intercalation cathodes through the generation of localized electron holes on oxygen. *Nat. Chem.* **2016**, *8* (7), 684−691.

(19) McCalla, E.; Abakumov, A. M.; Saubanère, M.; Foix, D.; Berg, E. J.; Rousse, G.; Doublet, M.-L.; Gonbeau, D.; Novák, P.; Van Tendeloo, G.; Dominko, R.; Tarascon, J.-M. Visualization of O-O peroxo-like dimers in high-capacity layered oxides for Li-ion batteries. *Science* **2015**, *350* (6267), 1516−1521.

(20) Sathiya, M.; Abakumov, A. M.; Foix, D.; Rousse, G.; Ramesha, K.; Saubanère, M.; Doublet, M. L.; Vezin, H.; Laisa, C. P.; Prakash, A. S.; Gonbeau, D.; VanTendeloo, G.; Tarascon, J. M. Origin of voltage decay in high-capacity layered oxide electrodes. *Nat. Mater.* **2015**, *14* (2), 230−238.
(21) Yan, P.; Zheng, J.; Tang, Z.-K.; Devaraj, A.; Chen, G.; Amine, K.; Zhang, J.-G.; Liu, L.-M.; Wang, C. Injection of oxygen vacancies in the bulk lattice of layered cathodes. *Nat. Nanotechnol.* **2019**, *14* (6), 602−608.
(22) Croy, J. R.; Garcia, J. C.; Iddir, H.; Trask, S. E.; Balasubramanian, M. Harbinger of hysteresis in lithium-rich oxides: Anionic activity or defect chemistry of cation migration. *J. Power Sources* **2020**, *471*, No. 228335.
(23) House, R. A.; Marie, J.-J.; Pérez-Osorio, M. A.; Rees, G. J.; Boivin, E.; Bruce, P. G. The role of O2 in O-redox cathodes for Li-ion batteries. *Nature Energy* **2021**, *6* (8), 781−789.
(24) Pearce, P. E.; Perez, A. J.; Rousse, G.; Saubanère, M.; Batuk, D.; Foix, D.; McCalla, E.; Abakumov, A. M.; Van Tendeloo, G.; Doublet, M.-L.; Tarascon, J.-M. Evidence for anionic redox activity in a tridimensional-ordered Li-rich positive electrode β-Li2IrO3. *Nat. Mater.* **2017**, *16* (5), 580−586.
(25) Perez, A. J.; Jacquet, Q.; Batuk, D.; Iadecola, A.; Saubanère, M.; Rousse, G.; Larcher, D.; Vezin, H.; Doublet, M.-L.; Tarascon, J.-M. Approaching the limits of cationic and anionic electrochemical activity with the Li-rich layered rocksalt Li3IrO4. *Nature Energy* **2017**, *2* (12), 954−962.
(26) Sathiya, M.; Rousse, G.; Ramesha, K.; Laisa, C. P.; Vezin, H.; Sougrati, M. T.; Doublet, M. L.; Foix, D.; Gonbeau, D.; Walker, W.; Prakash, A. S.; Ben Hassine, M.; Dupont, L.; Tarascon, J. M. Reversible anionic redox chemistry in high-capacity layered-oxide electrodes. *Nat. Mater.* **2013**, *12* (9), 827−835.
(27) Yamamoto, K.; Zhou, Y.; Yabuuchi, N.; Nakanishi, K.; Yoshinari, T.; Kobayashi, T.; Kobayashi, Y.; Yamamoto, R.; Watanabe, A.; Orikasa, Y.; Tsuruta, K.; Park, J.; Byon, H. R.; Tamenori, Y.; Ohta, T.; Uchimoto, Y. Charge Compensation Mechanism of Lithium-Excess Metal Oxides with Different Covalent and Ionic Characters Revealed by Operando Soft and Hard X-ray Absorption Spectroscopy. *Chem. Mater.* **2020**, *32* (1), 139−147.
(28) Rouxel, J. Some solid state chemistry with holes: Anion−cation redox competition in solids. *Curr. Sci.* **1997**, *73* (1), 31−39.
(29) Rouxel, J. Anion−Cation Redox Competition and the Formation of New Compounds in Highly Covalent Systems. *Chem. - Eur. J.* **1996**, *2* (9), 1053−1059.
(30) Lai, K. T.; Antonyshyn, I.; Prots, Y.; Valldor, M. Anti-Perovskite Li-Battery Cathode Materials. *J. Am. Chem. Soc.* **2017**, *139* (28), 9645−9649.
(31) Saha, S.; Assat, G.; Sougrati, M. T.; Foix, D.; Li, H.; Vergnet, J.; Turi, S.; Ha, Y.; Yang, W.; Cabana, J.; Rousse, G.; Abakumov, A. M.; Tarascon, J.-M. Exploring the bottlenecks of anionic redox in Li-rich layered sulfides. *Nature Energy* **2019**, *4* (11), 977−987.
(32) Hansen, C. J.; Zak, J. J.; Martinolich, A. J.; Ko, J. S.; Bashian, N. H.; Kaboudvand, F.; Van der Ven, A.; Melot, B. C.; Nelson Weker, J.; See, K. A. Multielectron, Cation and Anion Redox in Lithium-Rich Iron Sulfide Cathodes. *J. Am. Chem. Soc.* **2020**, *142* (14), 6737−6749.
(33) Goodenough, J. B.; Kim, Y. Locating redox couples in the layered sulfides with application to Cu [Cr2] S4. *J. Solid State Chem.* **2009**, *182* (10), 2904−2911.
(34) Martinolich, A. J.; Zak, J. J.; Agyeman-Budu, D. N.; Kim, S. S.; Bashian, N. H.; Irshad, A.; Narayan, S. R.; Melot, B. C.; Nelson Weker, J.; See, K. A. Controlling Covalency and Anion Redox Potentials through Anion Substitution in Li-Rich Chalcogenides. *Chem. Mater.* **2021**, *33* (1), 378−391.
(35) Leube, B. T.; Robert, C.; Foix, D.; Porcheron, B.; Dedryvère, R.; Rousse, G.; Salager, E.; Cabelguen, P.-E.; Abakumov, A. M.; Vezin, H.; Doublet, M.-L.; Tarascon, J.-M. Activation of anionic redox in d0 transition metal chalcogenides by anion doping. *Nat. Commun.* **2021**, *12* (1), 5485.
(36) Ravel, B.; Newville, M. ATHENA, ARTEMIS, HEPHAESTUS: data analysis for X-ray absorption spectroscopy using IFEFFIT. *Journal of synchrotron radiation* **2005**, *12* (4), 537−541.
(37) Kraft, S.; Stümpel, J.; Becker, P.; Kuetgens, U. High resolution x-ray absorption spectroscopy with absolute energy calibration for the determination of absorption edge energies. *Rev. Sci. Instrum.* **1996**, *67* (3), 681−687.
(38) Tang, W.; Sanville, E.; Henkelman, G. A grid-based Bader analysis algorithm without lattice bias. *J. Phys.: Condens. Matter* **2009**, *21* (8), No. 084204.
(39) Hetényi, B.; De Angelis, F.; Giannozzi, P.; Car, R. Calculation of near-edge x-ray-absorption fine structure at finite temperatures: Spectral signatures of hydrogen bond breaking in liquid water. *J. Chem. Phys.* **2004**, *120* (18), 8632−8637.
(40) Giannozzi, P.; Baroni, S.; Bonini, N.; Calandra, M.; Car, R.; Cavazzoni, C.; Ceresoli, D.; Chiarotti, G. L.; Cococcioni, M.; Dabo, I.; Dal Corso, A.; de Gironcoli, S.; Fabris, S.; Fratesi, G.; Gebauer, R.; Gerstmann, U.; Gougoussis, C.; Kokalj, A.; Lazzeri, M.; Martin-Samos, L.; Marzari, N.; Mauri, F.; Mazzarello, R.; Paolini, S.; Pasquarello, A.; Paulatto, L.; Sbraccia, C.; Scandolo, S.; Sclauzero, G.; Seitsonen, A. P.; Smogunov, A.; Umari, P.; Wentzcovitch, R. M. QUANTUM ESPRESSO: a modular and open-source software project for quantum simulations of materials. *J. Phys.: Condens. Matter* **2009**, *21* (39), 395502.
(41) Liang, Y.; Prendergast, D. Quantum many-body effects in x-ray spectra efficiently computed using a basic graph algorithm. *Phys. Rev. B* **2018**, *97* (20), No. 205127.
(42) Nagarajan, S.; Hwang, S.; Balasubramanian, M.; Thangavel, N. K.; Arava, L. M. R. Mixed Cationic and Anionic Redox in Ni and Co Free Chalcogen-Based Cathode Chemistry for Li-Ion Batteries. *J. Am. Chem. Soc.* **2021**, *143* (38), 15732−15744.
(43) Yabuuchi, N.; Yoshii, K.; Myung, S.-T.; Nakai, I.; Komaba, S. Detailed Studies of a High-Capacity Electrode Material for Rechargeable Batteries, Li2MnO3−LiCo1/3Ni1/3Mn1/3O2. *J. Am. Chem. Soc.* **2011**, *133* (12), 4404−4419.
(44) Marchini, F.; Saha, S.; Alves Dalla Corte, D.; Tarascon, J. M. Li-Rich Layered Sulfide as Cathode Active Materials in All-Solid-State Li−Metal Batteries. *ACS Appl. Mater. Interfaces* **2020**, *12* (13), 15145−15154.
(45) Ayama, T.; Tsukasaki, H.; Kawasaki, Y.; Nakajima, H.; Tatsumisago, M.; Sakuda, A.; Hayashi, A.; Mori, S. Microstructure and Charge−Discharge Mechanism of a Li3CuS2 Positive Electrode Material for All-Solid-State Lithium-Ion Batteries. *ACS Applied Energy Materials* **2021**, *4* (6), 6290−6295.
(46) Kang, K.; Ceder, G. Factors that affect Li mobility in layered lithium transition metal oxides. *Phys. Rev. B* **2006**, *74* (9), No. 094105.
(47) Bui, K. M.; Dinh, V. A.; Ohno, T. Diffusion Mechanism of Polaron−Li Vacancy Complex in Cathode Material Li2FeSiO4. *Applied Physics Express* **2012**, *5* (12), No. 125802.
(48) Maxisch, T.; Zhou, F.; Ceder, G. Ab initio study of the migration of small polarons in olivine LixFePO4 and their association with lithium ions and vacancies. *Phys. Rev. B* **2006**, *73* (10), No. 104301.
(49) Kim, S. S.; Agyeman-Budu, D. N.; Zak, J. J.; Dawson, A.; Yan, Q.; Cában-Acevedo, M.; Wiaderek, K. M.; Yakovenko, A. A.; Yao, Y.; Irshad, A.; Narayan, S. R.; Luo, J.; Nelson Weker, J.; Tolbert, S. H.; See, K. A. Promoting Reversibility of Multielectron Redox in Alkali-Rich Sulfide Cathodes through Cryomilling. *Chem. Mater.* **2022**, *34* (7), 3236−3245.
(50) Shi, D.-R.; Shadike, Z.; Wang, T.; Yang, S.-Y.; Xia, H.-Y.; Wang, Y.-K.; Yue, J.-L.; Hu, E.; Bak, S.-M.; Yue, X.-Y.; Zhou, Y.-N.; Ma, L.; Ghose, S.; Wu, T.; Zhang, Q.-H.; Xing, Z.; Zhang, Y.-N.; Zheng, L.; Gu, L.; Yang, X.-Q.; Fu, Z.-W. Reversible dual anionic-redox chemistry in NaCrSSe with fast charging capability. *J. Power Sources* **2021**, *502*, No. 230022.
(51) Blandeau, L.; Ouvrard, G.; Calage, Y.; Brec, R.; Rouxel, J. Transition-metal dichalcogenides from disintercalation processes. Crystal structure determination and Mossbauer study of Li2FeS2

and its disintercalates LixFeS2 (0.2⩽ x⩽ 2). *Journal of Physics C: Solid State Physics* **1987**, *20* (27), 4271.
(52) Brec, R.; Prouzet, E.; Ouvrard, G. Redox processes in the LixFeS2/Li electrochemical system studied through crystal, Mössbauer, and EXAFS analyses. *J. Power Sources* **1989**, *26* (3), 325−332.
(53) Dugast, A.; Brec, R.; Ouvrard, G.; Rouxel, J. Li2FeS2, a cathodic material for lithium secondary battery. *Solid State Ionics* **1981**, *5*, 375−378.
(54) Quilty, C. D.; West, P. J.; Li, W.; Dunkin, M. R.; Wheeler, G. P.; Ehrlich, S.; Ma, L.; Jaye, C.; Fischer, D. A.; Takeuchi, E. S.; Takeuchi, K. J.; Bock, D. C.; Marschilok, A. C. Multimodal electrochemistry coupled microcalorimetric and X-ray probing of the capacity fade mechanisms of Nickel rich NMC − progress and outlook. *Phys. Chem. Chem. Phys.* **2022**, *24* (19), 11471−11485.
(55) Blanchard, P. E. R.; Liu, S.; Kennedy, B. J.; Ling, C. D.; Zhang, Z.; Avdeev, M.; Jang, L.-Y.; Lee, J.-F.; Pao, C.-W.; Chen, J.-L. Studying the effects of Zr-doping in (Bi0.5Na0.5)TiO3via diffraction and spectroscopy. *Dalton Transactions* **2014**, *43* (46), 17358−17365.
(56) Cabaret, D.; Bordage, A.; Juhin, A.; Arfaoui, M.; Gaudry, E. First-principles calculations of X-ray absorption spectra at the K-edge of 3d transition metals: an electronic structure analysis of the pre-edge. *Phys. Chem. Chem. Phys.* **2010**, *12* (21), 5619−5633.
(57) Yoon, W.-S.; Balasubramanian, M.; Chung, K. Y.; Yang, X.-Q.; McBreen, J.; Grey, C. P.; Fischer, D. A. Investigation of the Charge Compensation Mechanism on the Electrochemically Li-Ion Deintercalated Li1-xCo1/3Ni1/3Mn1/3O2 Electrode System by Combination of Soft and Hard X-ray Absorption Spectroscopy. *J. Am. Chem. Soc.* **2005**, *127* (49), 17479−17487.
(58) Wang, T.; Ren, G.-X.; Shadike, Z.; Yue, J.-L.; Cao, M.-H.; Zhang, J.-N.; Chen, M.-W.; Yang, X.-Q.; Bak, S.-M.; Northrup, P.; Liu, P.; Liu, X.-S.; Fu, Z.-W. Anionic redox reaction in layered NaCr2/3Ti1/3S2 through electron holes formation and dimerization of S−S. *Nat. Commun.* **2019**, *10* (1), 4458.
(59) Farrell, S. P.; Fleet, M. E.; Stekhin, I. E.; Kravtsova, A.; Soldatov, A. V.; Liu, X. Evolution of local electronic structure in alabandite and niningerite solid solutions [(Mn,Fe)S, (Mg,Mn)S, (Mg,Fe)S] using sulfur K- and L-edge XANES spectroscopy. *Am. Mineral.* **2002**, *87* (10), 1321−1332.
(60) Wu, Z. Y.; Ouvrard, G.; Lemaux, S.; Moreau, P.; Gressier, P.; Lemoigno, F.; Rouxel, J. Sulfur K-Edge X-Ray-Absorption Study of the Charge Transfer upon Lithium Intercalation into Titanium Disulfide. *Phys. Rev. Lett.* **1996**, *77* (10), 2101−2104.
(61) Wang, T.; Ren, G.-X.; Xia, H.-Y.; Shadike, Z.; Huang, T.-Q.; Li, X.-L.; Yang, S.-Y.; Chen, M.-W.; Liu, P.; Gao, S.-P.; Liu, X.-S.; Fu, Z.-W. Anionic Redox Regulated via Metal−Ligand Combinations in Layered Sulfides. *Adv. Mater.* **2022**, *34* (4), No. 2107353.
(62) Hyler, F. P.; Wuille Bille, B. A.; Ortíz-Rodríguez, J. C.; Sanz-Matias, A.; Roychoudhury, S.; Perryman, J. T.; Patridge, C. J.; Singstock, N. R.; Musgrave, C. B.; Prendergast, D.; Velázquez, J. M. X-ray absorption spectroscopy insights on the structure anisotropy and charge transfer in Chevrel Phase chalcogenides. *Phys. Chem. Chem. Phys.* **2022**, *24* (28), 17289−17294.
(63) Wan, L. F.; Wright, J.; Perdue, B. R.; Fister, T. T.; Kim, S.; Apblett, C. A.; Prendergast, D. Revealing electronic structure changes in Chevrel phase cathodes upon Mg insertion using X-ray absorption spectroscopy. *Phys. Chem. Chem. Phys.* **2016**, *18* (26), 17326−17329.
(64) Wang, T.; Ren, G.-X.; Xia, H.-Y.; Shadike, Z.; Huang, T.-Q.; Li, X.-L.; Yang, S.-Y.; Chen, M.-W.; Liu, P.; Gao, S.-P.; Liu, X.-S.; Fu, Z.-W. Anionic Redox Regulated via Metal−Ligand Combinations in Layered Sulfides. *Advanced Materials* **2022**, *34* (4), No. 2107353.
(65) Pickering, I. J.; Brown, G. E.; Tokunaga, T. K. Quantitative Speciation of Selenium in Soils Using X-ray Absorption Spectroscopy. *Environ. Sci. Technol.* **1995**, *29* (9), 2456−2459.
(66) Olegario, J. T.; Yee, N.; Miller, M.; Sczepaniak, J.; Manning, B. Reduction of Se(VI) to Se(-II) by zerovalent iron nanoparticle suspensions. *J. Nanopart. Res.* **2010**, *12* (6), 2057−2068.
(67) Lebert, B. W.; Balédent, V.; Toulemonde, P.; Ablett, J. M.; Rueff, J.-P. Emergent high-spin state above 7 GPa in superconducting FeSe. *Phys. Rev. B* **2017**, *97*, No. 180503.
(68) Joseph, B.; Iadecola, A.; Simonelli, L.; Mizuguchi, Y.; Takano, Y.; Mizokawa, T.; Saini, N. L. A study of the electronic structure of FeSe1 − xTex chalcogenides by Fe and Se K-edge x-ray absorption near edge structure measurements. *J. Phys.: Condens. Matter* **2010**, *22* (48), 485702.
(69) Yamamoto, T. Assignment of pre-edge peaks in K-edge x-ray absorption spectra of 3d transition metal compounds: electric dipole or quadrupole? *X-Ray Spectrometry* **2008**, *37* (6), 572−584.
(70) Shadike, Z.; Zhou, Y.-N.; Chen, L.-L.; Wu, Q.; Yue, J.-L.; Zhang, N.; Yang, X.-Q.; Gu, L.; Liu, X.-S.; Shi, S.-Q.; Fu, Z.-W. Antisite occupation induced single anionic redox chemistry and structural stabilization of layered sodium chromium sulfide. *Nat. Commun.* **2017**, *8* (1), 566.

https://doi.org/10.1021/acs.chemmater.4c00854
Chem. Mater. 2024, 36, 8623−8638